MASTER COPY

REPORT DOCUMENTATION PAGE		Form Approved OMB NO. 0704-0188

Public reporting burden for this collection of information is estimated to average 1 hour per response, including the time for reviewing instructions, searching existing data sources, gathering and maintaining the data needed, and completing and reviewing the collection of information. Send comment regarding this burden estimates or any other aspect of this collection of information, including suggestions for reducing this burden, to Washington Headquarters Services, Directorate for Information Operations and Reports, 1215 Jefferson Davis Highway, Suite 1204, Arlington, VA 22202-4302, and to the Office of Management and Budget, Paperwork Reduction Project (0704-0188), Washington, DC 20503.

1. AGENCY USE ONLY (Leave blank)	2. REPORT DATE December 15, 1999	3. REPORT TYPE AND DATES COVERED Final Report, 01/21/97 - 01/20/00

4. TITLE AND SUBTITLE Hot Carrier Thermometry in Heterostructures. Carrier Heating in Semiconductor Lasers.	5. FUNDING NUMBERS DAAG55-97-1-0009
6. AUTHOR(S) Dr. Gregory Belenky	

7. PERFORMING ORGANIZATION NAMES(S) AND ADDRESS(ES) The Research Foundation of State University of New York Office of Research Services Stony Brook, New York 11794-3366	8. PERFORMING ORGANIZATION REPORT NUMBER

9. SPONSORING / MONITORING AGENCY NAME(S) AND ADDRESS(ES) U.S. Army Research Office P.O. Box 12211 Research Triangle Park,, NC 27709-2211	10. SPONSORING / MONITORING AGENCY REPORT NUMBER ARO 34604.13-EL

11. SUPPLEMENTARY NOTES

The views, opinions and/or findings contained in this report are those of the author(s) and should not be construed as an official Department of the Army position, policy or decision, unless so designated by other documentation.

12a. DISTRIBUTION / AVAILABILITY STATEMENT Approved for public release; distribution unlimited.	12b. DISTRIBUTION CODE

13. ABSTRACT (Maximum 200 words)

We consider both theoretically (intersubband lasers) and experimentally (bipolar double heterostructure laser) the physical phenomena responsible for the carrier heating effect. Electron relaxation by polar excitation (LO-phonons and plasmons) was studied as a key process which determines the high-temperature operation of intersubband lasers. A simplified model for intrawell LO-phonon-assisted relaxation processes in an asymmetric one-well/one-barrier intersubband laser heterostructure was developed. A new relaxation channel for high-energy electrons by transverse plasmon-like collective excitations in intersubband laser heterostructures was predicted. It was shown that in an active quantum well with inverted subband occupation the nonequilibrium character of intersubband plasmons results in strong peculiarities of the light-emission spectra: the intersubband resonance screening of light-wave electric field leads to both narrowing and anomalous downshift of the optical gain spectrum. It was experimentally proved that suppression of the thermionic emission of electrons from the active region of bipolar MQW double heterostructure lasers leads to improvement of the device performance within a wide temperature range. We demonstrate for the first time the possibility to predict (by simulation) the "optimum" p-i junction placement in 1.3 μm InGaAsP/InP MQW lasers. Such "optimum" p-i junction placement simultaneously maximizes the external efficiency and minimizes the device threshold current.

14. SUBJECT TERMS Semiconductor lasers, carrier heating effect		15. NUMBER IF PAGES
		16. PRICE CODE

17. SECURITY CLASSIFICATION OR REPORT UNCLASSIFIED	18. SECURITY CLASSIFICATION OF THIS PAGE UNCLASSIFIED	19. SECURITY CLASSIFICATION OF ABSTRACT UNCLASSIFIED	20. LIMITATION OF ABSTRACT UL

NSN 7540-01-280-5500

Standard Form 298 (Rev. 2-89)
Prescribed by ANSI Std. 239-18
298-102

Enclosure 1

HOT CARRIER THERMOMETRY IN HETEROSTRUCTURES
CARRIER HEATING IN SEMICONDUCTOR LASERS

FINAL PROGRESS REPORT

DR. GREGORY BELENKY

Associate Professor

January 21, 1997 – January 20, 2000

U.S. ARMY RESEARCH OFFICE

DAAG 55-97-1-0009

THE RESEARCH FOUNDATION OF THE STATE UNIVERSITY OF NEW YORK

AT STONY BROOK

OFFICE OF RESEARCH SERVICES

APPROVED FOR PUBLIC RELEASE

DISTRIBUTION UNLIMITED

20000628 039

TABLE OF CONTENTS

HOT CARRIER THERMOMETRY IN HETEROSTRUCTURES. CARRIER HEATING IN SEMICONDUCTOR LASERS

HOT CARRIER THERMOMETRY IN HETEROSTRUCTURES
CARRIER HEATING IN SEMICONDUCTOR LASERS

STATEMENT OF THE PROBLEM

Heating of the carriers in the active region is an important issue for both interband and intersubband semiconductor lasers. In this work we consider both theoretically (intersubband lasers) and experimentally (bipolar double heterostructure laser) the physical phenomena responsible for the carrier heating effect.

In the first part of this project we carry out theoretical investigation of unipolar quantum cascade lasers. Electron relaxation by polar excitations (LO-phonons and plasmons) is a key process which determines the high-temperature operation of these novel devices. The polar excitation spectrum in the many-interface laser heterostructures was calculated in the framework of the dielectric continuum model. Intra- and intersubband nonradiative scattering processes responsible for the excessive injection current level in these devices were considered. Both LO-phonon and plasmon assisted electron relaxation is considered taking into account the effect of polar-mode confinement in the thin-layer laser heterostructures.

In the second part of the present work we demonstrate (experimentally and as a result of simulation) that suppression of the thermionic emission of electrons from the active region of bipolar double heterostructure lasers leads to improvement of the device performance. We study both experimentally and theoretically how the change of the p-doping profile, particularly the p-i junction placement, affects the output characteristics of 1.3 µm InGaAsP/InP MQW lasers. Simulated device characteristics include carrier transport, the capture of carriers into the quantum wells, the quantum mechanical calculation of the properties of the wells, and the solution for the optical mode and its population self-consistently as function of diode bias.

We study the telecommunication interband 1.3µm InGaAsP/InP MQW lasers. The choice was based on the extreme maturity of technology of InGaAsP/InP laser

heterostructures. All devices studied in this work were grown and fabricated at Lucent Bell Laboratories.

I. ELECTRON RELAXATION IN INTERSUBBAND SEMICONDUCTOR LASERS

Introduction

Intersubband semiconductor lasers (ISLs) are of great interest for mid-infrared device applications. As compared to interband midinfrared (led salt) lasers, the unipolar intersubband lasers have the advantage of a higher temperature operation. Since its first implementation in 1994 (Faist 1994), the quantum cascade laser (QCL), has been demonstrated to operate at room temperature within the wavelength range 5-8 μm (Capasso 1999). Optically pumped "three-level-type" intersubband lasers have been also proposed and investigated (Sun 1993; Gauthier-Lafaye, 1997). In both schemes, electrons are injected or optically pumped to a high-energy level of the heterostructure and the light-emitting transition takes place between this and the next lower subband. The energy separation between these levels, and thus the emitted light wavelength, can be controlled by varying the widths of the wells and barriers. Besides the energy levels, the designer can control transition matrix elements (Capasso 1997), electron-phonon scattering rates (Stroscio 1996), and electron lifetimes in active subbands (Capasso 1996).

Spectral dependence of the material gain is the main characteristic of an ISL heterostructure and is determined primarily by the electron energy spectrum and electron distribution function in the active region. Electron distribution in ISL is substantially non-equilibrium since there is an inherent source of electron (and phonon) heating: the energy released during the intersubband and intrasubband nonradiative electron relaxation processes. Due to larger intersubband separation the heating effects are more pronounced in the ISL heterostructures designed for short-wavelength operation (4-5 μm). The heating effects influence the gain spectra of the ISL in a nontrivial way. The result depends crucially on the balance between the two major interactions in the system, which are electron-LO-phonon and electron-electron (plasmon) interactions.

If the threshold current and, consequently, the electron concentration is sufficiently low ($n \sim 10^{10}$ cm^{-2}) the main relaxation process in the ISL active region is electron-LO-phonon interaction. The distribution functions in lasing subbands are

4

nonequilibrium and nonthermal (Gorfinkel 1996). The maximum optical gain is achieved at short wavelength edge of the spectral line, which corresponds, to the lasing transition between subband bottoms. After the nonradiative intersubband transition the electrons cascade down the lower lasing subband and can escape the active quantum well by the interwell tunneling. Both processes are assisted by LO-phonon emission. As a result, the gain spectrum becomes sensitive to the details of the electron – phonon interaction and lasing action depends significantly on the modified LO-phonon spectrum of the many-interface ISL heterostructure (Kisin 1997).

In the opposite limit of high electron concentration ($n > 10^{11}$ cm^{-2}) the electron-electron interaction becomes efficient channel for the relaxation processes in active region of ISL. Since polar excitations provide the most effective mechanism for this relaxation, the electron thermalization in this limit is affected both by LO-phonons and plasmons. Like LO-phonon spectrum, plasmon spectrum is significantly influenced by confinement effect in many-interface heterostructures. Longitudinal 2D-plasmons with square-root dispersion participate in intrasubband relaxation whereas intersubband collective excitations (intersubband plasmons) with energy of the order of intersubband energy separation can influence the intersubband relaxation.

In this chapter we aim to study the most important features of the electron relaxation, which govern the subband population dynamics in the active region of the intersubband semiconductor lasers.

1. Effect of the LO-phonon confinement on electron relaxation in many-interface laser heterostructures

Polar interaction with long-wavelength longitudinally polarized optical (LO) phonons is a topic of continuing interest, since electron inter- and intrasubband relaxation in quantum well heterostructures are governed primarily by this scattering mechanism. During the last decade, the importance of optical phonon confinement and localization effects has been discussed widely in literature. Both macroscopic (Mori 1989) and microscopic (Rucker 1992) approaches of electron-optical-phonon interactions have been used to show that in polar semiconductor heterostructures, the interaction of confined

electrons with polar optical phonons is modified strongly compared to the three-dimensional case. The LO phonon scattering was shown to be important in narrow quantum well heterostructures designed for injection or optically pumped laser applications (Sun 1993; Stroscio 1996; Kisin 1997). Photoexcited carrier relaxation processes in coupled quantum wells (Educato 1993) and phonon-assisted tunneling in double-barrier heterostructures (Turley 1994) were described successfully taking into account the existence of interface optical-phonon modes.

All of the above treatments applied to highly symmetric structures such as quantum wells, double-well or double-barrier heterostructures. Recently, another kind of heterostructures has appeared in which an accurate description of the electron-LO-phonon interaction is of prime importance. The active region of the unipolar quantum cascade laser (Faist 1994) incorporates a combination of a quantum well with an adjacent narrow barrier layer providing the electron tunneling escape from the active quantum well after a light-emitting transition; see Fig. I.1.1. For this three-interface configuration, the interface phonon potential distributions should differ substantially from the well-known solutions for symmetric heterostructures with an even number of interfaces (Mori, 1989; Stroscio, 1996; Kim, 1992). In the latter case, the phonon potential distributions usually are characterized by definite parity providing well-known parity selection rules for electron inter- and intrasubband transitions (Jain, 1989). In a three-interface heterostructure with a sufficiently narrow barrier layer, the parity based selection rules do not hold for intrawell electron transitions. This circumstance combined with the growing complexity of the spectrum of interface optical phonon modes in multiple heterointerface structures (Yu, 1997) gives rise to substantial difficulties in theoretical analysis of electron relaxation processes. In this work, we show that the total rate of intrawell electron relaxation by interface phonons in three-interface heterostructures is practically independent of the barrier width; this permit us to use the phonon spectrum of a single quantum well for the description of more complex cascade heterostructures. Simultaneously, we show that any attempt to exploit the simpler bulk-like phonon spectrum fails if the electron kinetic energy is of the order of the typical phonon energy in the heterostructure. The macroscopic dielectric continuum model (Mori, 1989) is used in

this chapter for the description of the polar-optical-phonon modes; this has been shown to agree well with microscopic calculations (Huang, 1988; Rucker, 1992).

We consider the simplest three-interface combination of a quantum well with an adjacent narrow barrier layer as in Fig. I.1.1. Index $i = 0 \div 3$ numerates here the layers of the heterostructure. In cascade laser heterostructures, layers 0 and 3 represent the same layer, which can be designed as a gradual alloy or a superlattice. Under an applied electric field, this layer provides flat-band condition for electron transport from one cascade to the next. The length of this region is usually longer then the active quantum well width, a, and its exact structure does not influence the intrawell electron relaxation processes considered in this article. Therefore, we represent the layers 0 and 3 as half-spaces of wide-gap and narrow-gap semiconductors, respectively.

In dielectric continuum model, the optical phonon spectrum of a heterostructure includes interface phonon modes and confined LO-phonon modes which are approximated as being completely confined to the corresponding layer (well or barrier) and not affected by or coupled to the adjacent layer. The frequency of each interface mode is split according to different frequency ranges of optical phonons in the constituent materials. This splitting is influenced also by the type of materials used in the heterostructure, which usually are binary materials or ternary alloys. For the sake of simplicity, we consider here a binary material heterostructure assuming GaAs as the well material and AlAs as the barrier, wide-gap semiconductor. In the case of binary materials, the dielectric functions in the barrier (b) and the well (w) heterostructure layers are

$$\varepsilon_{b,w}(\omega) = \varepsilon_{b,w\infty} \frac{\omega^2 - \omega_{lb,w}^2}{\omega^2 - \omega_{tb,w}^2} \ . \tag{I.1.1}$$

Following the transfer matrix method (Yu, 1997), we can obtain the dispersion equation for a three-interface heterostructure in the form:

$$\frac{\varepsilon_b(\omega)}{\varepsilon_w(\omega)} = \xi_m \quad , \quad m = \text{outer, inner} ; \tag{I.1.2}$$

where,

$$\xi_{outer} = -1 \ ; \tag{I.1.3}$$

$$\xi_{inner(S,A)} = -\xi_0 \pm \sqrt{\xi_0^2 - 1} < 0 \ ; \ \xi_0 = \frac{2}{(1 - e^{-2qa})(1 - e^{-2qb})} - 1. \tag{I.1.4}$$

7

Here, q is the in-plane phonon wave vector. Relations (2,3) give us two dispersionless solutions with constant frequencies equal to the frequencies of the two single-interface phonon modes of the GaAs/AlAs heterointerface. As we show below, these modes tend to localize in the vicinity of the outer heterointerfaces (#1 or #3) and may be considered to be outer interface modes. Relations (2,4) in the limit b>>a, lead to the dispersion equation of a simple double heterostructure (quantum well) (Mori, 1989). Consequently, we obtain two different types of inner modes, which can be classified as symmetric (S) or antisymmetric (A) according to their behavior in this limit. In expression (4), the sign (+) relates to the symmetric and the sign (−) relates to the antisymmetric inner interface mode. By analogy with the outer mode, each inner mode is split in frequency according to the two optical phonon frequency ranges in constitutive materials. For binary materials, these dispersion relations can be easily obtained analytically by substituting dielectric function (1) into the dispersion equation (2):

$$\omega^2_{m(b,w)} = \Omega^2_m \pm \left(\Omega^2_m - \frac{\omega^2_{lb}\omega^2_{tw} + \chi_m \omega^2_{lw}\omega^2_{tb}}{1 + \chi_m} \right)^{1/2} ; \quad \binom{b}{w} \rightarrow \binom{+}{-} ; \quad (\text{I.1.5})$$

$$\Omega^2_m = \frac{\omega^2_{lb} + \omega^2_{tw} + \chi_m(\omega^2_{lw} + \omega^2_{tb})}{2(1 + \chi_m)} ; \quad \chi_m = -\frac{\varepsilon_{w\infty}}{\varepsilon_{b\infty}}\xi_m > 0 .$$

Here, the sign (+) corresponds to index b - that is to the phonon frequency range of barrier material - and the sign (−) should be chosen for phonon frequency range of well material (index w). For ternary alloys, this classification scheme remains the same except for additional mode splitting. The calculated dispersion curves for interface phonon modes in a binary GaAs/AlAs heterostructure are presented in Fig. I.1.2a.

For a three-interface heterostructure, the interface phonon potential distribution takes simple analytical form:

$$\varphi_{m,q}(z) = A_m \left(\frac{\hbar}{\varepsilon_0 q} \right)^{\frac{1}{2}} \left(\frac{\partial \varepsilon_b(\omega)}{\partial \omega} - \xi_m \frac{\partial \varepsilon_w(\omega)}{\partial \omega} \right)^{-\frac{1}{2}} f_m(z), \quad (\text{I.1.6})$$

$$f(z) = \sum_{i=0}^{3} [C_{i1}e^{q(z_i - z)} + C_{i2}e^{q(z - z_{i+1})}]_{z_i < z < z_{i+1}} .$$

The coefficients in (6) are given by,

$$A_{outer} = \left(\frac{e^{2qa}}{e^{2qa} + e^{2qb} - 1} \right)^{\frac{1}{2}} \; ; \qquad C_i = \begin{pmatrix} C_{i1} \\ C_{i2} \end{pmatrix}; \qquad (I.1.7)$$

$$C_0 = \begin{pmatrix} 0 \\ 1 \end{pmatrix}; \; C_1 = \begin{pmatrix} 1 \\ 0 \end{pmatrix}; \; C_2 = \begin{pmatrix} 0 \\ e^{q(b-a)} \end{pmatrix}; \; C_3 = \begin{pmatrix} e^{q(b-a)} \\ 0 \end{pmatrix}.$$

for outer interface mode, and

$$A_{inner} = \left(\frac{1}{2} \frac{e^{2qb} - 1}{e^{2qa} + e^{2qb} - 1} \right)^{\frac{1}{2}} \; ; \qquad (I.1.8)$$

$$C_0 = \begin{pmatrix} 0 \\ 1 \end{pmatrix}; \; C_1 = \frac{1}{2} \begin{pmatrix} 1 - \xi \\ (1+\xi)e^{qa} \end{pmatrix};$$

$$C_2 = \begin{pmatrix} (\xi + \xi_0)\sinh qa \\ -\dfrac{e^{qa}}{2\sinh qb} \end{pmatrix}; \; C_3 = \begin{pmatrix} (\xi - 1)e^{-qb}\sinh qa \\ 0 \end{pmatrix}$$

for inner phonon modes. As in the case of one- and two-interface heterostructures, these distributions do not depend on the type of constitutive materials. For ternary alloys, we simply have to use the two-pole approximation for the corresponding dielectric function (1). As a result, the introduction of a ternary alloy as a barrier or well material does not alter the functional form of the interface modes but modifies the coefficient for the mode strength according to the change in the dielectric function. The exemplary phonon potential distributions are presented in Fig. I.1.3.

Fig. I.1.3a shows the characteristic behavior of the inner and outer optical-phonon modes in a three-interface heterostructure. In the limit $b \gg a$, the outer mode tends to localize on the right outer interface (#3), whereas the inner modes relate to the well-known symmetric and antisymmetric interface modes in a double heterostructure. If the barrier width, b, becomes comparable with well width, a, the inner modes are substantially perturbed but their basic symmetry features still remain; see Fig. I.1.3b. The outer mode now represents the symmetrized linear combination of the single interface modes of the left and right outer interfaces (#1 and #3). If $a = b$, this combination is exactly symmetric. Further decrease of the barrier width b gives rise to a potential redistribution of the outer interface modes from interface #3 toward the interface #1. At

9

the same time, the inner phonon modes switch to the barrier layer, simultaneously changing their symmetry; see Fig. I.1.3c.

To characterize the individual phonon mode strengths, we can introduce the coupling coefficients, β_m, for the electron-phonon interactions, normalizing the phonon envelopes, $\varphi_m(z)$, in (6) according to the condition $\int \tilde{\varphi}^2(z)dz = 1$. The interaction Hamiltonian is represented in the form,

$$H_{el-ph} = \sum_{m,q} \beta_m(q)\tilde{\varphi}_{m,q}(z)\frac{e^{iqr}}{\sqrt{S}}\left(\hat{a}_{m,q} + \hat{a}^+_{m,-q}\right). \tag{I.1.9}$$

Here, S is the cross-sectional area of the heterostructure. For nonnormalized potentials (6), we would use the elementary electron charge, e, instead of coupling constants, β_m. The q-dependence of β_m in the three-interface system is similar to that obtained in the work by Turley for the case of a symmetric double-barrier heterostructure (Turley, 1994). The coupling constants of the outer interface modes (Ob, Ow) diverge as $1/q$ for small phonon wave vectors, q. The coupling constants for the LO-like inner phonon modes (IAw, ISb) diverge as $1/\sqrt{q}$, whereas for two TO-like inner modes (IAb, ISw) they tend to go to zero at small values of q. At larger q, all the coupling coefficients converge to the values of the corresponding coupling constant for the single interface mode in the phonon energy ranges of the barrier (b) or the well (w) semiconductor materials; see Fig. I.1.2b. However, the coupling constants by itself cannot give us the most or the least important phonon modes in the scattering process. The overlap integrals between the phonon potential and electron wave functions significantly influence the scattering rates and should be calculated with great care. Since the inclusion of the subband nonparabolicity is essential for correct description of electron states, we calculate the electron energy spectrum on the basis of the four-band Kane model taking into account the complex boundary conditions for multicomponent wave functions (Kisin, 1998). The calculations have been restricted to the case of a quantum well with a square well potential profile and a well width, $a = 6$ nm. We use this electron energy spectrum for all scattering rate calculations represented here neglecting the perturbing action of heterointerface #3 onto the electron wave functions in quantum well. For barrier width

$b > 2$ nm, this approximation is quite reasonable due to the high-energy band offsets $\Delta_{c,v}$ at the AlAs/GaAs heterointerface and, consequently, due to the small penetration of the electron wave function into the barrier region even for high-energetic states in second subband.

For a heterostructure with large barrier width $b \gg a$, the rates for intrawell scattering processes should be close to the rates in a single quantum well. Parity-selection rules for inner interface mode scattering hold strictly in this limit. Thus, symmetric inner interface and even-parity confined modes dominate in the intrasubband scattering whereas antisymmetric inner interface and odd-parity confined modes contribute primarily to the intersubband transitions. For large b, outer interface mode locates at the remote heterointerface #3 and can not participate to intrawell electron transitions because of the small overlap with the electron states. However, if the well and barrier layer dimensions are comparable, the outer mode scattering becomes dominant in accordance with growing overlap integral and as a result of the higher coupling constant. Correspondingly, the scattering rates by the inner interface modes diminish since these modes switch to the barrier layer. Fig. I.1.4 illustrates this behavior for intrasubband 2-2 and intersubband 2-1 electron transitions. Here, scattering rates by interface optical phonons are represented as functions of the barrier width. The scattering rate is computed using the Fermi golden rule. The electron kinetic energy has been chosen so that $E_2 = 60$ meV in order to include the interaction with all possible interface modes. Fig. I.1.5 shows the energy dependence of the total intrasubband 1-1 scattering rates for heterostructures with $b = 3, 6$, and 12 nm (curves 1). It is readily seen that the previously mentioned mutual redistribution of the outer and inner phonon modes makes the total interface phonon scattering rate practically independent on barrier width over the entire range of electron kinetic energy.

A qualitative explanation of this result may be related to the sum rule established for the electron-phonon interaction in heterostructures (Rücker, 1992; Register, 1992). Inasmuch as the wave functions of initial and final electron states are confined in the same layer of the heterostructure (quantum well layer in this case) we can divide the total

11

of the squared matrix elements for the scattering processes into two parts, corresponding to the interaction with the interface and confined phonons:

$$\sum_{\text{all modes}} |M_m|^2 = \sum_{\text{interface}} |M_i(a,b)|^2 + \sum_{\text{confined}} |M_c(a)|^2 = \sum_{\text{bulk}} |M_b(a)|^2. \qquad (\text{I.1.10})$$

Neglecting the phonon energy dispersion, this total should be the same for any complete and orthogonal set of phonon modes; in particular, it equals the sum of matrix elements of the interaction with effective LO bulk phonons. However, for confined electron states, neither the second sum nor the right-hand side of equation (10) depend on the barrier width b because of the strong damping of electron states in the barrier region. Consequently, we can expect the first sum (for interface modes) to be independent of b as well. It is worth emphasizing that for the interwell or the phonon assisted escape processes the situation can be quite different especially in the case of resonance transitions (Stroscio, 1996). Here, the proper design of the phonon potential distribution for a given barrier width may appear necessarily to achieve high subband depopulation rate.

For injected and/or hot electrons in the active quantum well of the laser heterostructure, the electron kinetic energy is usually comparable with the LO phonon energy. The condition $E_{kin} \approx \hbar\omega_{ph}$ separates active and passive regions in accordance with optical phonon emission process and determines the electron distribution function in the low-concentration limit. It is important to realize that just in this electron energy range we cannot substitute the complex phonon spectrum of the heterostructure with bulk phonons of any constituent material. In Fig. I.1.5 we compare the intrasubband 1-1 scattering rates calculated for three different phonon spectrum models. Here, curves 1 represent the total scattering rate due to the combined action of all interface, confined, and barrier phonon modes in the heterostructures with different values of barrier width, b. Two other curves have been obtained by approximating the complex phonon spectrum of the heterostructure with bulk phonons of well (curve 2) or barrier (curve 3) material. In the electron energy range where the phonon energy is crucial for the scattering rate value, the results of the three models differ significantly. Only if the electron kinetic energy exceeds the highest phonon energy in the system we can use the quasibulk approximation suggesting some intermediate composition for the effective bulk

12

semiconductor material. The basis of this approximation is that the total of the matrix elements always falls between the corresponding values for bulk well and bulk barrier materials (Rücker, 1992); this situation is illustrated in Fig. I.1.6. It is seen, however, that this total is substantially different for different values of phonon wave vector q. Therefore, since the emission scattering rates for different phonon modes depend on the phonon energy stepwise, we cannot choose the unique effective quasi-bulk approximation in the whole range of different scattering processes and have to use more complex phonon spectrum. In this work, we have shown that for the three-interface heterostructures, an adequate model of the phonon spectrum is given by the phonon spectrum of a single quantum well.

In conclusion, polar electron-optical-phonon interaction in an asymmetric three-interface heterostructure - quantum well plus adjusted barrier layer of finite width, b - has been studied. The interface phonon spectrum of the heterostructure is found to consist of three basic types of modes. Two of the interface modes in the limit of large barrier width can be related to symmetric and antisymmetric solutions for an isolated quantum well and have similar dispersion. The third interface mode represents a symmetrized linear combination of single interface modes of the outer heterointerfaces. We have shown that the individual phonon potential distributions in the three-interface heterostructure are substantially modified when changing layer dimensions. The decrease of the barrier width, b, gives rise to the redistribution of the outer interface mode potential from the right outer interface (between barrier layer and half-space narrow gap semiconductor) toward the left outer interface (between barrier half-space and well layer). At the same time, both inner phonon modes switch to the barrier layer simultaneously changing their symmetry. We have found that this mutual redistribution of interface modes keeps the total electron-optical-phonon scattering rate practically unchanged for initial and final electron states localized in the quantum well region. This enables us to use the simpler phonon spectrum of a single quantum well for the analysis of intrawell electron relaxation in the three-interface heterostructures used in cascade laser design. The applicability of the sum rule for scattering rate calculation has been examined by comparing the total scattering rate by all interface and confined optical phonons with the results obtained in the quasibulk approximation for the phonon

13

spectrum. We show that in the case of injected or hot electrons with kinetic energy comparable to the typical energy of optical phonons, the quasibulk approximation cannot be used for accurate calculation of the electron-phonon scattering rates in heterostructures.

2. Other polar excitations – confined plasmon modes and resonant screening in intersubband laser heterostructures

In this section we consider the electron-plasmon interaction and intersubband resonance screening in a quantum well with inverted subband occupation typical for intersubband lasers. We show that in such a system the intersubband plasmon emission leads to an efficient de-excitation of the nonequilibrium initial electron state and raises the occupation of states in the lower subband. Downshift and resonance narrowing of the intersubband optical emission spectra are obtained and shown to be influenced by the process of intersubband plasmon excitation.

Relaxation of nonequilibrium charge carriers is important for the performance of many electron heterostructure devices. At low sheet electron concentrations $N_s \leq 10^{12} cm^{-2}$, the intrasubband relaxation in A_3B_5 heterostructures is determined basically by polar optical phonon and intrasubband-plasmon scattering processes, which become comparable at the level of electron concentration $N_s \approx 10^{11} cm^{-2}$ (Das Sarma, 1996). In laser heterostructures designed for optical transitions in the range $\hbar\omega \approx 150$-300 meV the relevant energy quanta, $\hbar\omega_{ph}$ and $\hbar\omega_{pl}^{(11)}$, are small compared with the subband separation Δ_{21}, so that nonequilibrium electrons entering the first subband after intersubband 2-1 phonon-emission transitions must subsequently cascade down the first subband (Faist, 1996) emitting the optical phonons and low-energy intrasubband plasmons. The high-energy intersubband plasmon mode, $\omega_{pl}^{(12)}$, being characterized by an antisymmetric potential distribution, could participate in the intersubband relaxation causing electron intersubband 2-1 transitions with a small momentum transfer. However, under the condition of Fermi-filling of the first subband states, this kind of transition

14

becomes possible only for high-energy electrons in the second subband because of the up-shift of the energy of the intersubband collective excitations (plasmons) (Allen, 1976)

$$\hbar\omega_{pl}^{(12)}(q) \approx \Delta_{21} + \delta_q \; ; \quad \delta_q = \frac{e^2 N_s S}{\kappa_0 \kappa}\left(1 + O(qa)\right). \qquad (I.2.1)$$

Here, δ_q and S are, respectively, the depolarization shift of the intersubband excitation energy and depolarization integral, κ is the dielectric constant. As a result, for electrons injected into the bottom of the second subband the plasmon-assisted intersubband relaxation is negligible.

The above picture of the relaxation process has been developed for the normal ordering of subband filling when most of electrons occupy the lower subband states, $N_s \approx n_1$. The operation of the quantum cascade laser (Faist, 1994) requires a nonequilibrium state of the active quantum well with a significant population in the upper (second) subband, $N_s = n_1 + n_2$, including the situation with inverted subband occupation, $n_2 > n_1$. We demonstrate here that the inverted order of subband occupation results in a novel effective relaxation mechanism for nonequilibrium electrons in the lower subband due to scattering by intersubband plasmon excitations of the upper-subband electrons. In contrast to the cascade relaxation by phonons and intrasubband plasmons, this one-step scattering process efficiently fills the lower subband bottom and should be taken into consideration if one is interested in the realization of a high-gain QCL in the low-concentration regime (Gorfinkel 1996).

We restrict ourselves to the two lowest parabolic subbands characterized by a Fermi-distributed population in the upper subband $N_s \approx n_2$ with the Fermi wave vector k_F and Fermi energy ε_F. The intersubband plasmon potential $\varphi_{pl}^{(21)}(z, \mathbf{r}, t) = \varphi_{21}(z) e^{i\mathbf{q}\mathbf{r}} \cos\omega t$ causes polarization of the electronic system in the second subband corresponding to the admixture of lower energy states $\psi_1(z)$ from the first subband to the occupied second subband states $\psi_2(z)$. In the rotating wave approximation the density response at the perturbation frequency ω is

$$\rho_q^{(21)}(z, \mathbf{r}, t) \approx -n_2 e^2 \frac{\langle \psi_2(z) | \varphi_{21}(z) | \psi_1(z) \rangle}{\hbar\omega - \Delta_{21}} \psi_2(z)\psi_1(z) e^{i\mathbf{q}\mathbf{r}} \cos\omega t. \qquad (I.2.2)$$

15

Using this induced charge distribution as a source in Poisson's equation (Allen 1976) we easily determine the intersubband plasmon energy $\hbar\omega_{pl}^{(21)}(q) \approx \Delta_{21} - \delta_q$. This quantum turns out to be smaller than $\hbar\omega_{pl}^{(12)}$ due to the positive sign of the electric field energy, which is a part of the energy of the collective intersubband excitation. In contrast to the system with normal subband occupation (Fig. I.2.1a), where the intersubband plasmon excitation raises the ground state energy E_0 by intersubband plasmon quantum, the polarization process (2) results in the *lowering* of the energy of the initial nonequilibrium state (Fig. I.2.1b). As a result, the scattering process with intersubband plasmon emission in the inverted system must include the intersubband 1-2 electron transition associated with the absorption of the de-excitation energy $\hbar\omega_{pl}^{(21)}$. For this scattering process, the initial and final state energies, $E_i = E_0 + \varepsilon_1(k)$ and $E_f = E_0 + \Delta_{21} + \varepsilon_2(\mathbf{k} - \mathbf{q}) - \hbar\omega_{pl}^{(21)}(q)$, are related by the conservation law, which imposes a threshold for the allowed kinetic energy values of scattered electrons, viz. $\varepsilon_1 \geq \varepsilon_{th} \approx \varepsilon_F + \delta_0$. In accordance with the random phase approximation (RPA), the state of the inverted system with one excited intersubband plasmon can be represented as $\left| E_0 - \hbar\omega_{pl}^{(21)}(q) \right\rangle = \sum F(k)\hat{c}_{1,\mathbf{k}+\mathbf{q}}^+ \hat{c}_{2,\mathbf{k}} \left| E_0 \right\rangle$. The expectation value of the first-subband number operator in this state is then $\left\langle \hat{c}_{1,\mathbf{k}}^+ \hat{c}_{1,\mathbf{k}} \right\rangle = \left| F(\mathbf{k} + \mathbf{q}) \right|^2$, where the form-factor $F(k)$ obeys the normalization condition $\sum |F(k)|^2 = 1$. This implies an effective increase of the first subband occupation by one electron. Since $q \ll k_F$ this process fills the bottom states of the first subband - to a good approximation uniformly.

Consider now the simplest model of intersubband relaxation for nonequilibrium electrons coming to subband 1 from subband 2 after the emission of an optical phonon. We suppose the depopulation of the first subband be fast tunneling events, $\tau_{1out} \ll \tau_{ph}^{(21)}$. Then, in a steady state one has $n_1 \approx n_2 \tau_{1out} / \tau_{ph}^{(21)} \ll n_2$, whence the electron-plasmon scattering rates are determined essentially by the electron concentration

in the second subband. The balance equation for the electrons occupying the bottom of the first subband (with partial concentration n_0) can be written in the form,

$$\frac{m}{\pi\hbar^2} \int_{\varepsilon_{th}}^{\Delta-\hbar\omega_{ph}} d\varepsilon_1 \frac{f(\varepsilon_1)}{\tau_{pl}^{(21)}(\varepsilon_1)} = \frac{n_0}{\tau_{1out}} \,, \qquad (I.2.3)$$

where $f(\varepsilon_1)$ is the electron distribution function in the first subband, normalized as

$$\frac{m}{\pi\hbar^2} \int_{\varepsilon_F}^{\Delta-\hbar\omega_{ph}} d\varepsilon_1 f(\varepsilon_1) = n_1 - n_0; \quad f(\varepsilon_1 < \varepsilon_F) = f_0 \approx \frac{\pi\hbar^2 n_0}{m\varepsilon_F} \,, \qquad (I.2.4)$$

and $1/\tau_{pl}^{(21)}$ - is the electron scattering rate by intersubband plasmons, $\omega_{pl}^{(21)}$. In the high-energy region, $\varepsilon_F < \varepsilon_1 < \Delta_{21}$, the distribution function $f(\varepsilon_1)$ is established by optical phonon and intrasubband-plasmon-cascade emission and can be approximated by the simple expression (Gorfinkel 1996):

$$f(\varepsilon_1) \propto \exp\left(-\frac{\Delta_{21} - \hbar\omega_{ph} - \varepsilon_1}{W_{cc}\tau_{1out}}\right), \qquad (I.2.5)$$

where $W_{cc} = W_{ph}^{(11)} + W_{pl}^{(11)}$ is the total cascade cooling rate for 1-1 intrasubband relaxation processes. For an exemplary calculation, we consider an infinitely deep quantum well with subband energy separation $\Delta_{21} = 300$ meV and width $a = 4$ nm. All material parameters correspond to $Ga_{0.47}In_{0.53}As$. The scattering rates, $1/\tau_{pl,ph}$, have been calculated for $T = 0$ K by the standard method using the dielectric continuum model (Constantinou 1991). The cooling rates, $W_{ph,pl}$, are estimated upon inserting the corresponding energy quantum inside the integral in the Fermi golden rule. To simplify the model, the phonon spectrum has been approximated by bulk phonons though phonon confinement may be important for exact quantitative description of electron relaxation processes in thin quantum wells (Kisin 1997; 1998). The electron concentration range is chosen to be 5×10^{10} to $5 \times 10^{11} cm^{-2}$, which is typical for the QCL (Faist 1994). Phonon-plasmon coupling becomes important at higher concentration level $N_s \geq 10^{12} cm^{-2}$ (Das Sarma 1996) and is neglected here. Fig. I.2.2 represents the distribution function for the electron population in the first subband calculated for two

values of electron sheet concentration, N_s. Two separate groups of electrons are readily seen in the first subband: "cool" electrons in the subband bottom and "hot" electrons in high-energy states characterized by the distribution function (5). The inverted population of the high-energy states is formed by cascade-like emission of optical phonons and intrasubband plasmons, whereas the subband bottom states with $k \leq k_F$ are filled mostly due to the one-step events of intersubband plasmon excitation. We would like to emphasize that the latter process effectively fills precisely those states which are the final states for light-emitting transitions (states with $k \leq k_F$ in the model considered here), restricting to some extent the value of inverted population associated with laser action. This trend becomes more pronounced if the depopulation time, τ_{1out}, increases. It has been suggested by V.F. Elesin and Yu. V. Kopaev (Elesin 1995) that cascade relaxation process due to optical phonon emission does not lead to a substantial electron population in the first subband bottom ($\varepsilon_1 < \hbar\omega_{ph}$) unless the subband separation is an integer number of optical phonon quanta. It has been claimed, therefore, that under certain conditions higher depopulation time of the lower subband, τ_{1out}, may be beneficial for enhanced laser characteristics in cascade intersubband devices. Unfortunately, significant occupation of the bottom states with $k < k_F$ resulting from intersubband plasmon emission invalidates this idea. The inset in Fig. I.2.2 shows the occupation number f_0 for the bottom states in the first subband as a function of the electron concentration n_2, calculated for two different values of depopulation time, τ_{1out}, namely, 1 and 2 psec. For shorter τ_{1out} the effect of subband bottom filling by the intersubband plasmons becomes less important.

We now turn to the optical characteristics in the quantum well, which are substantially influenced by the intersubband plasmon spectrum. In a system with normal ordering of the subband occupation the light-wave field screening by the electron gas leads to an up-shift in the energy of the intersubband absorption spectrum (Allen 1976; Vinter 1977). At high electron concentrations the absorption line-width is considerably narrower than the single particle broadening determined by the nonparabolicity of the subbands (Ando 1978; Zaluzny 1991). We will show that for a quantum well with inverted subband occupation the depolarization field associated with the nonequilibrium

intersubband plasmon excitations, $\omega_{pl}^{(21)}$, leads to a down-shift of emission peak and a corresponding down-shift and narrowing of the optical gain spectra. For a two-subband model, following (Zaluzny 1991) we obtain low-temperature long-wavelength susceptibility $\chi(\omega, q \to 0)$, which includes the depolarization-field effect, under the condition of inverted subband population and determines the optical gain:

$$g(\omega) = \frac{\omega}{c\sqrt{\kappa_\infty}} \mathrm{Im}\, \chi(\omega, 0) \;;\quad \chi(\omega) = \frac{e^2 z_{12}^2 n_2}{2\pi\Delta_{21}\kappa_0}(1 - f_0)\frac{G(\omega)}{1 - \alpha G(\omega)} \;; \qquad (\text{I.2.7})$$

$$G(\omega) = \frac{\Delta_{21}}{\varepsilon_F}\int_0^{\varepsilon_F}\frac{\Omega_\varepsilon d\varepsilon_2}{\Omega_\varepsilon^2 - \hbar^2\omega^2 - 2i\hbar^2\omega\gamma} \;;\quad \alpha = (n_2 - n_0)\frac{2e^2 S}{\Delta_{21}\kappa_0\kappa}(1 - f_0) \;.$$

Here $\Omega_\varepsilon = \Delta_{21} + \varepsilon_2 - \varepsilon_1$ is the energy separation for a particular "vertical" transition and γ is polarization dephazing rate, which we assume to be a constant (Ando, 1978). The dipole matrix element z_{12} and the depolarization integral S are also assumed to be k- independent; in a two-subband model with infinitely deep quantum well they equal, respectively, $16a/9\pi^2$ and $5a/9\pi^2$. In the case of normal subband occupation, the parameter α in (11) changes sign and we arrive at the results of Zaluzny and Warburton for optical absorption (Zaluzny, 1991; Warburton, 1996). The factor $(1 - f_0)$ describes effect of the first subband bottom filling, which in our model occurs due to the nonequilibrium intersubband plasmon excitation.

In Figure I.2.3 we show the results of exemplary gain spectra calculations. If the depolarization effect is neglected ($\alpha = 0$, dashed curves), the line-width increases significantly with the electron concentration due to lower transition energies contributing to the spontaneous emission process. At higher temperatures this nonparabolicity-induced single-particle broadening would be even more pronounced. Taking into account the resonance screening of the light field (solid curves) we obtain a substantial downshift of the gain peak position and the line narrowing analogous to that observed in absorption spectra (Warburton 1996). The line-width at the half-maximum level is practically "pinned" at the value $2\hbar\gamma$. This agrees well with the experimental observations of the narrow spontaneous emission line-width even for high-temperature operating QCL-heterostructures (Sirtori 1996; Gmachl 1998). Our results show also the remarkable

influence of the lower subband bottom filling on the gain peak position. The maximum shift of the gain spectrum is achieved at low value of depopulation time $\tau_{1out} \approx 0.1$ psec, which is typical for modern QCL design, while the increase of τ_{1out} leads to a more effective filling of subband bottom (see Fig. I.2.2) and results in substantial decrease of the peak shift.

In conclusion, it is demonstrated that the polar-mode scattering processes in ISL active region with inverted subband occupation differ significantly from those in normal systems. The excitation of intersubband plasmons lowers the energy of the nonequilibrium initial state and opens a new relaxation channel for high-energy electrons in the lower subband. In this process the scattered electron undergoes a transition to the higher subband while the bottom of the lower subband is filled as a result of intersubband plasmon excitation. This one-step scattering process requires small momentum transfer and is more efficient than the cascade relaxation by phonons or intrasubband plasmons. In quantum wells with an inverted subband occupation the nonequilibrium character of intersubband plasmons results in strong peculiarities of the light-emission spectra. We have shown that the intersubband resonance screening of light-wave electric field in these systems leads to both narrowing and anomalous downshift of the optical gain spectrum. Peak position of the optical gain is affected significantly by the change of the first subband occupation due to the intersubband plasmon excitation.

II. STUDIES OF THE ELECTRON THERMIONIC EMISSION FROM ACTIVE REGION OF InGaAsP/InP MQW LASERS (EXPERIMENT AND MODELING)

Intoduction

Despite the industrial success of strained multi-quantum-well (MQW) InGaAsP/InP laser heterostructures, a search for ways to improve the temperature performance of these lasers remains one of the most important directions in reducing the cost of devices that emit at a wavelength of 1.3μm and operate reliably over the temperature range of - 40 to +85C. Modern lasers based on the InGaAsP/InP material system are characterized by high temperature sensitivity of their characteristics. This fact stems from poor electron confinement due to a small conduction band offset in the conventional InGaAsP/InP system and high values of the working injection current

density of multi-quantum-well devices (Anthony, 1980; Agrawal, 1986). The high intensity of thermionic emission of the electrons from active region of the lasers responsible for device high temperature sensitivity as well as for high value of the threshold current. It was predicted theoretically and shown experimentally (Chen, 1983; Kazarinov, 1994; Belenky, 1995) that an increase of acceptor concentration in the p-cladding layer adjacent to the active region in 1.3μm bulk active InGaAsP/InP lasers minimizes the voltage drop at the p-cladding/SCH interface and avoids a substantial reduction of the barrier for thermionic emission of electrons from the active region layer.

In this work we study both experimentally and theoretically how the change of the p-doping profile, particularly the p-i junction placement, affects the output characteristics of 1.3 μm InGaAsP/InP MQW lasers. Device characteristics are simulated including carrier transport, capture of carriers into the quantum wells, the quantum mechanical calculation of the properties of the wells, and the solution for the optical mode and its population self-consistently as a function of diode bias.

1. Carrier leakage current and effect of the electrostatic band profile deformation inInGaAsP/InP MQW lasers.

In this work the temperature dependencies of the threshold current, device slope efficiency and heterobarrier electron leakage current from the active region of InGaAsP/InP MQW lasers with different profiles of acceptor doping were measured under pulse injection within the temperature range of 10 - 80 °C and the range of injection current densities up to 10 kA/cm². This level of the injection is close to operating conditions of 1.3 μm MQW InGaAsP/InP buried heterostructure devices.

We have fabricated and measured broad area laser devices which incorporate an electron collector (Belenky, 1995; 1996) for leakage measurements with the cavity length of 500 μm, mesa width of 20 μm and collector area about 5μm × 5μm. For measurements of the device slope efficiency, we used broad area lasers with 60 μm stripe width and the same cavity length. Lasers with three different p-doping profiles in the vicinity of the active region were studied: with an undoped p-cladding/SCH interface, with moderately Zn doped interface (~$5 \times 10^{17} cm^{-3}$) and doped interface ($1.5 \times 10^{18} cm^{-3}$). Zn concentration at the SCH/active region interface was about $10^{16} cm^{-3}$ for the first type of devices and did

not exceed 10^{17}cm^{-3} for both latter types. The laser active region consists of 9 quantum wells 70 A thick separated by 100 A barriers and is surrounded by 500 A separate confinement layers ($\lambda = 1.15$ µm). The device structure and its doping profiles were not different from those described in (Belenky, 1996). In our studies the injection current pulses have a 50 ns - 250 ns width and a 100 kHz - 1 kHz repetition rate.

Fig. II.1.1 shows the temperature dependence of threshold current density J_{th} for devices with the different profiles of p-doping. One can see that the values of threshold currents in 1.3 µm InGaAsP/InP lasers and their temperature dependencies are different for devices with different Zn doping profiles. In lasers with an undoped p-cladding/SCH interface, the threshold current rapidly increases with temperature above 40 ^{0}C. The temperature dependence of J_{th} for devices with a moderately doped p-cladding/SCH interface or with a doped interface are characterized by one slope with typical $T_0 = 60$ K. Thickness of the cladding layers of the devices studied in this work were 0.65µm, almost twice thinner that it is necessary to avoid absorption of the optical field by alloyed contacts and so to optimize the external quantum efficiency value. Measured at 20C value of η_{ext} for devices with moderately doped and doped p-doping/SCH interface was about 25% and for devices with undoped interface 20%. We observed a strong dependence of η_{ext} temperature sensitivity on doping profile. Fig. II.1.2 presents the results of measurements of temperature dependencies of external efficiency for devices with different doping profiles.

The results of measurements of the heterobarrier carrier leakage current J_L are presented in Fig. II.1.3a and Fig. II.1.3b for devices with undoped and doped interfaces correspondingly. We used a purely electrical technique (Chen, 1983) to measure the leakage of electrons from the active region of a InGaAsP/InP MQW laser. The obtained results in their entirety demonstrate unambiguously that optimization of the p-doping profile allows to decrease the electron leakage current in InGaAsP/InP lasers by about one order of magnitude. However, the results of the J_L measurements cannot explain the difference in the dependencies η_{ext} (T) for devices with different doping profiles presented in Fig. II.1.2. As shown in Fig. II.1.3, the measured value of J_L does not exceed 4% of the total injection current densities even for devices with an undoped p-cladding/SCH interface at 80 ^{0}C. Taking into account that the collection efficiency of

22

leakage current density by the electron collector on the top of the p-contact is at least 80% (Belenky, 1995), we can estimate that the maximum possible contribution of the effect of heterobarrier leakage to the reduction of internal efficiency is about 5%. For lasers with a doped interface, the corresponding values are less than 0.5% at 80 ^{0}C. Comparison of the results presented in Fig. II.1.1,2 with Fig. II.1.3 allows us to conclude that the rapid increase of the threshold current and the decrease of efficiency with temperature for 1.3 μm InGaAsP/InP MQW lasers with an undoped p-cladding/SCH interface cannot be explained by the increase of leakage current. The qualitative understanding of the results presented in Fig. II.1.1-3 can be achieved in the framework of the model of electrostatic band profile deformation developed in (Seki, 1995; Garbuzov, 1995) for MQW InP based lasers.

At high injection, electrons can spill over into the SCH region from the QW's, while holes remain localized within the QW. This separation of charges creates electrostatic band profile deformation making the energy of the effective barrier for the conduction band larger, and that for the valence band smaller compared with the initial one. At elevated temperatures, the hole density within the SCH can increase leading to an increase in loss and recombination in the SCH, and as a result causing the rise of the threshold current and the decrease of the slope efficiency (Seki, 1995a; 1995b). The results of calculation of the dependencies η_{ext}(T) and I_{th}(T) carried out within the framework of the model of the electrostatic band profile deformation appear to be in good agreement with measured η_{ext}(T) and I_{th}(T) for MQW InGaAsP/InP lasers (Seki, 1995b). It was shown that the rapid rise of the I_{th} with temperature within the region 40-80^{0}C, which is a common phenomenon for undoped lasers (Fig. II.1.1), is caused mostly by the effect of electrostatic band profile deformation and not by the increase with temperature of the intensity of Auger processes. The conclusion (1995a) about accumulation of holes in the SCH layer at elevated temperatures is supported by the results of spectrally resolved measurements of the spontaneous emission from the SCH layer of 1.3 μm InGaAsP/InP MQW lasers (Bemussi, 1995). It was shown that above threshold, in agreement with prediction (Seki, 1995a,b), the intensity of radiative recombination in the SCH layer of these lasers increases with the drive current and that this increase correlates quantitatively with the decrease of the device slope efficiency.

To explain the difference in measured dependencies $\eta_{ext}(T)$ and $I_{th}(T)$ for devices with different acceptor doping shown in Fig. II.1.1,2 in the framework of the model (Seki, 1995a,b; Garbuzov, 1995), we assume that doping profile affects the charge distribution within the SCH, thus suppressing the influence of the band bending effect on device performance. The difference in dependencies $\eta_{ext}(T)$ and $I_{th}(T)$ for devices with a moderately Zn doped interface and doped interface can also be explained by the difference in optical loss caused by the degree of p-doping. Assumption about suppression of the effect of electrostatic band bending by incorporation of acceptors into the SCH layer allows us to understand the difference in dependencies $J_L(J_I)$ presented in Fig. II.1.3a and Fig. II.1.3b for devices with different doping profiles. Increase of the electron energy barrier for thermionic emission caused by the electrostatic band bending effect can be responsible for sublinear character of the dependencies $J_L(J_I)$ registered in the case of undoped heterointerface structure (Fig. II.1.3a). Fig. II.1.4a and Fig. II.1.4b show the dependencies of the coefficient $(1 - J_L/J_I)$ versus current density J_I for devices with undoped and doped interfaces correspondingly. The value of this coefficient characterizes the contribution of heterobarrier leakage current change with injection current into the dependence of the device internal quantum efficiency on injection current. The parameter σ defined by equation: $\eta_{int}(I_{inj}) = \eta_{int}^{th} - \sigma(I_{inj} - I_{th})$ characterizes the contribution of the total leakage current (in the case of the buried heterolasers it is the sum of the heterobarrier and blocking layer leakage) in the change of the device internal efficiency with injection current, here η_{int}^{th} is internal quantum efficiency at threshold. For 1.3μm InGaAsP/InP MQW buried heterolasers devices common value of the σ is about 0.5a^{-1} (Zhang, 1995). Our experiments show that for devices with moderately doped and doped p-doping/SCH interface contribution of the heterobarrier leakage in σ doesn't exceed 0.1 even at 80C. We can conclude that optimization of p-doping allows to minimize the contribution of heterobarrier leakage effect into the σ.

In summary of this part, we demonstrate that the temperature sensitivity of the device characteristics depends on the profile of p-doping, and that variation in the temperature behavior of the device threshold current and slope efficiency for lasers with different doping profiles cannot be explained by the change of the measured value of the

leakage current with doping only. The obtained experimental results can be qualitatively explained by suggesting that doping can affect the value of electrostatic band profile deformation which affects temperature sensitivity of the output device characteristics. We demonstrate that utilizing a p-doped p-cladding/SCH layer interface in InGaAsP/InP multi-quantum-well lasers leads to improved device temperature performance even at 80^0C and high injection current densities.

2. Optimum placement of the p-i junction in InGaAsP/InP MQW lasers. Balance between carrier leakage and free carrier absorption. Experiment and modeling

In this part we study MQW InGaAsP/InP lasers. As in previous section we will use optimization of Zn doping profile as a powerful technological method to control device performance. In this particular case to control the placement of the p-i junction. It is well known that fabrication of a 1.3 -1.5 μm wavelength separate confinement capped mesa buried heterostructure (CMBH) involves three growth steps: the growth of the base structure which is followed by mesa delineation and growth of current blocking layers (second epitaxial growth) and, finally, by cladding and contact layers (third growth) (Zilko, 1989; Swamatanian, 1995; Swamatanian, 1996). Zn is a commonly used p-type dopant in InGaAsP/InP lasers. It has been shown that in the process of fabrication of CMBH lasers the diffusion of Zn during third (final) growth plays a decisive role in the formation of the final doping profile of Zn in the vicinity of the laser active layer and in material electro-optical characteristics (Swamatanian, 1995, 1996; Schubert, 1995). This profile determines a variety of fundamental laser characteristics including the device gain, optical losses and leakage current as well as the device temperature and high frequency performance. One of the important problems of semiconductor laser engineering and technology is developing a tool for determining the optimum depth of the p-doping profile for lasers with a given design. In this work we study both experimentally and theoretically how the change of the p-doping profile, particularly the p-i junction placement, affects the output characteristics of 1.3 μm InGaAsP/InP MQW lasers.

We grew base structures of 1.3 μm InGaAsP/InP MQW lasers with three different doping profiles and fabricated broad area lasers. Part of the same wafers was used to

grow an additional p-cladding and contact layers (imitation of the third growth in the case of CMBH lasers) to fabricate lasers. As a result, we have established (a) the relationship between the epitaxial growth p-doping profile before and after regrowth, (b) the relationship between changes in the doping profile and the devices output characteristics. The simulations predict and the experiments show that an optimum p-i junction placement simultaneously maximizes external efficiency and minimizes threshold current. These facts can be used to optimize the p-doping profile of the device with a given design taking into account possible laser applications. It is demonstrated that tuning of the base epitaxial growth Zn profile allows one to fabricate MQW devices with a threshold current of approximately 80 A/cm^2 per well for devices with 9 QWs at room temperature or lasers with characteristic temperature $T_0 = 70$ K within the temperature range of 20 - 80°C.

InGaAsP/InP heterostructures were grown by low pressure (60 torr) metalorganic chemical vapor deposition (MOCVD) on (100) n$^+$-InP substrates. The strained MQW region consisted of nine 70 A wells and 100 A barriers in which the wells were mismatched ~ 1%. The separate confinement and contact layers were lattice matched. Fabricated structures are shown schematically in Fig. II.2.1(a,b). In part of the wafer, the contact layers were removed by etching, and another 1.2 μm of InP cladding was grown with an InGaAs contact layer on top (Fig. II.2.1(b)). The second growth was carried out at the temperature of 650^{0}C. Secondary ion mass spectrometry (SIMS) concentration depth profiles in the vicinity of the device active region for structures (Fig. II.2.1 (a)) prior to regrowth are shown in Fig. II.2.2 (a), and are referred to as structures (1), (2) and (3). While the As profiles are only shown in arbitrary units to denote placement of the MQW/SCH region, the Zn and Si profiles are quantitative. Fig. II.2.2(b) demonstrates the SIMS data obtained from structures (1) - (3) after the InGaAs contact layer was removed by etching and an additional 1.2 μm Zn doped InP and 0.2 μm contact layers were grown. These structures are labeled (4), (5) and (6), correspondingly. Significant changes in the Zn profiles from the regrowth procedure are easily recognizable.

The important parameter of the structures under consideration is the setback distance Δ between the p-doping profile edge for a Zn concentration 5 10^{17}cm^{-3} and the p-cladding/SCH interface (denoted by As in Fig. II.2.2). This setback is positive for a low

doped interface and negative for high p-doping of the SCH, that is Zn has penetrated the active region. We measured the temperature dependence of threshold current $I_{th}(T)$ and external efficiency η_{ext} for broad area devices with a cavity length of 500 µm and mesa width of 125 µm. In our studies the injection current pulses have a 50 ns width and a 100 kHz repetition rate. It is clear in Fig. II.2.3 (a, b)) that I_{th} as well as its temperature dependence both changed as a result of regrowth. The insert of Fig. II.2.3b shows the improvement of the characteristic temperature T_o (temperature range of 10 to 80°C) with doping at the heterointerface. Laser structure (4) demonstrates at room temperature the lowest threshold current of approximately 80 A/cm² per quantum well. However, these lasers with an undoped SCH layer are characterized by a rapid increase of threshold current for temperatures higher than 50°C. All devices with a doped p-SCH layer (structures (2), (3), (5) and (6)) exhibit only one slope for I_{th} (T) within the temperature range of 20 - 80°C (T_o = 65 - 70 K) and demonstrate a slightly higher I_{th} than for device (4). We used a direct electrical technique (Belenky, 1995, 1996) to measure heterobarrier leakage of electrons from the device active region and a modified Anderkson technique (Shtengel, 1995) to measure the total optical loss for CMBH devices.

There are competing effects, which are strongly influenced by the doping profile. First, the doping near the p-cladding to p-SCH heterointerface has a strong influence on the electron leakage out of the active layer affecting the device injection efficiency (Kazarinov, 1994). Second, the p-doping contributes to optical loss through the intervalence band absorption. Thirdly, the doping profile can modify the details of the carrier distribution in the multiquantum well region. This is a more subtle effect concerning the balance between the three dimensional carriers in the active region and the carriers confined to the quantum wells. It has also been argued (Donetsky, 1998) that doping can suppress the effect of band profile deformation in the SCH (Yamanaka, 1993; Seki, 1995) and alter the degree to which carriers spill out of the quantum wells.

In order to understand these effects in more detail, careful simulations have been performed. The simulations include normal carrier transport, the optical field, the bound carrier populations in each well, gain from the quantum wells and stimulated emission self consistently. In particular, the quantum wells are explicitly treated, including the quantum mechanical calculation of the bound levels, the densities of states and the gain.

Capture of carriers into the bound population is treated as a local recombination process for the three dimensional carriers. The transverse mode is based on solution of the Helmholtz equation including changes in refractive index induced by the free carriers. Further technical details of the simulation are described in (Alam, 1997; Hybertsen, 1998a, 1998b). Wide area diodes have been studied following the basic features of the samples under study. Mirror loss of 25 cm^{-1} is included. No scattering loss is considered. The loss due to the p-doping and the free carrier loss are both computed self-consistently from the hole distribution using measured coefficients (Henry, 1983). Coefficients for Auger recombination are in the range from values in the literature. In the simulations, the doping profile is constructed with idealized abrupt steps. The background doping in the active region was assumed to be n-type 10^{16} cm^{-3} for positive setback and p-type for negative setback.

Fig. II.2.4 shows the band diagram and quasi-Fermi levels (pertaining to the three dimensional carriers) for a broad area laser diode at high bias. The assumed p-doping profile ends 50 nm outside the p-side SCH. Electron leakage consists of thermionic emission over the heterobarrier and minority carrier diffusion to the p-contact. The effective barrier combines the band offset and the local band bending:

$$J_{leak} \propto \exp(-(E_c^{max} - F_n)/kT)$$

where F_n is the electron quasi-Fermi level in the SCH near the interface. The local maximum in the conduction band profile includes band bending related to the local doping concentration and the influence of any local voltage drop. The local voltage drop is dominated by the variation in the hole quasi-Fermi level, ΔF_p, illustrated in Fig. II.2.4. Under conditions of current injection, it can be argued that ΔF_p is approximately proportional to log(1+J/J$_0$) (Kazarinov, 1994). The scale J$_0$ is related to the local doping concentration in the p-cladding near the interface with larger doping giving a larger value of J$_0$. A detailed expression for J$_o$ is given in (Kazarinov, 1994). Higher doping near the interface reduces the heterobarrier leakage. If, furthermore, the carrier population in the active layer is clamped above threshold, then F_n is constant. It then follows that the leakage current is approximately proportional to the total current above threshold. However, in a multiquantum well laser, the situation is more complex. The three dimensional carriers are a reservoir which feeds the quantum wells supplying the gain for

28

stimulated emission. In this situation, the three dimensional population may not be fully clamped. Then the leakage current can be a superlinear function of the injection current.

The lower panel in Fig. II.2.4 shows the free carrier densities. The influence of carrier transport through the multiquantum well active region, particularly holes, is seen in the non-uniform electron density. Correspondingly, the bound hole population (in the wells) also vary. The bound hole population is larger for the well nearer to the p-side SCH. This has been described in more detail elsewhere (Alam, 1997; Hybertsen 1998a,b). Another feature of the self-consistent band profile in the active region is the substantial electron and hole densities in the p-side SCH ($\sim 5 \times 10^{17}$ cm^{-3}). This was also observed in quasiequilibrium calculations (Yamanaka 1993; Seki 1995). If the interface and the SCH are p-doped, then the light line in the upper panel shows that the band profile is significantly different. In particular, a higher barrier is presented for electron leakage. The carrier density in the p-side SCH (not shown) is lower and the amount of excess voltage near the interface is much smaller. This leads to much lower leakage in this case, consistent with (Kazarinov, 1994).

Dependencies of the measured and calculated coefficient J_L/J_I (J_L and J_I are leakage and injection currents correspondingly) on the setback are presented in Fig. II.2.5. Changes of this coefficient reflect a change in injection efficiency. Agreement between experiment and theory is satisfactory. This confirms the dependence of heterobarrier leakage on setback and shows that the simulation accurately models this effect.

The presence of higher doping near the active layer increases the optical loss. Experimental data for a CMBH device with cavity length 300μm and mesa width 1 μm were obtained by modified Andrekson technique (Shtengel 1995). The results of these loss measurements for devices with a doped SCH and with doped active regions are presented in Fig. II.2.6. The increase of the doping in the active shows a systematic increase in the optical loss. However, the change in optical loss with current below threshold shows approximately the same slope. The results of the simulation for the case of a doped SCH are also shown in Fig. II.2.6. The simulation is in approximate agreement with the experimental data. In particular, the change in optical loss with current derives from intervalence band absorption caused by the accumulation of bound

holes in the quantum wells. The calculated three-dimensional carriers in the active region are shown in Fig.II.2.4. These holes also contribute, but to a lesser extent.

Having considered the leakage and the optical loss separately, we now turn to the balance between these effects on device performance. The threshold condition is simply

$$g = \alpha_{mir} + \alpha_{scat} + \alpha_{dop} + \alpha_{fc}$$

where the contributions to the loss are due to the mirror, scattering, doping and free carriers. In a simple model, the threshold includes both the injection efficiency and the threshold carrier concentration in the active region:

$$I_{th} = \frac{1}{\eta_{inj}} \left(BN_{th}^2 + CN_{th}^3 \right)$$

where the injection efficiency and the conventional spontaneous emission and Auger coefficients enter. If the p-doping is low in the InP near the SCH, then the contribution to the loss from α_{dop} is low. However, the leakage current will be larger. On the other hand, moving the doping closer to the interface, or even into the active region, will optimize the leakage giving a near unity injection efficiency at the expense of a larger contribution from α_{dop}. In considering the balance of these factors, one must note that the threshold current rises superlinearly with loss but only linearly with injection efficiency. Further, the injection efficiency is no longer increasing once the interface is doped. However, p-doping in the active region still increases the loss. The influence of the p-doping on the quantum well populations is a more subtle point requiring detailed calculations. Finally, the net impact on threshold and external efficiency must be calculated in detail. The simulated diode performance as a function of p-doping setback is shown in Fig. II.2.7. The trade-off between leakage and optical loss is seen to result in a shallow minimum in the threshold current and a pronounced maximum in the external efficiency. In the limit of large positive setback, leakage eventually dominates over the reduction in loss. For negative setback, leakage is negligible. However, losses continue to rise with increased doping of the active.

The data in Fig. II.2.8 for devices before and after regrowth show that both the threshold current and the device external efficiency show optimum values for a setback of ~ 50 nm. The relative change in efficiency is well reproduced by the simulation. However, the experimental data suggest a much sharper optimum in threshold current

30

than does the theory. The absolute magnitude of the calculated threshold current is reasonable given that no parameters were specifically tuned for this purpose. Of more concern is the weak change in the calculated threshold current as the losses rise for negative setback. Concerning the two sets of devices measured, the difference in p-cladding thickness may be important. For the devices with thin p-cladding, the role of the metallization in the optical losses may be larger.

Beyond the physical effects of the doping profile already included, there may be other effects caused by Zn doping. This is more speculative, but these were not accounted for in the calculations. Impurity scattering can influence the intensity of the nonradiative losses in the active and the SCH layers. For example, the Auger coefficients may depend on the local doping concentration. Impurity scattering may also play some role in the calculation of the optical gain.

In conclusion, we have shown that details of the p-doping profile have systematic impact on the static device performance. In particular, there is an optimal placement for the p-i junction which both minimizes threshold and maximizes external efficiency. Detailed simulation shows that this is the balance between leakage current and optical loss. These considerations must be taken into account in the laser design for different applications.

EXECUTIVE SUMMARY

1. We show that optical phonon confinement effect is an important issue for correct calculation of the electron relaxation rates in intersubband semiconductor laser heterostructures. A simplified model for intrawell LO-phonon-assisted relaxation processes in an asymmetric one-well/one-barrier intersubband laser heterostructure has been developed. The practical invalidity of the bulk-like phonon spectrum approximation is demonstrated.

2. A new relaxation channel for high-energy electrons in intersubband laser heterostructures has been predicted. We show that one-step scattering by transverse plasmon-like collective excitations is more efficient than the cascade relaxation by LO-phonons or longitudinal intrasubband plasmons. We have shown that in an active quantum well with inverted subband occupation the nonequilibrium character of intersubband plasmons results in strong peculiarities of the light-emission spectra: the intersubband resonance screening of light-wave electric field leads to both narrowing and anomalous downshift of the optical gain spectrum.

3. We demonstrate for the first time the possibility to predict the "*optimum*" p-i junction placement in semiconductor laser diodes. Such "*optimum*" placement corresponds to the minimum of the intensity of thermionic emission of electrons from laser active region and simultaneously to the minimum of free carrier absorption. The simulations predict and the experiments confirm that the "*optimum*" p-i junction placement simultaneously maximizes external efficiency and minimizes threshold current. Tuning the device Zn profile we fabricated InGaAsP/InP MQW lasers with a world record value of the threshold current -80 A/cm^2 per well for devices with 9 QWs at room temperature and lasers with characteristic temperature $T_0 = 70$ K within the temperature range of 20 - 80°C.

FIGURE CAPTIONS

Figure I.1.1.

Schematic plot of conduction band profile of the three-interface heterostructure discussed in this study.

Figure I.1.2.

Interface phonon mode (a) dispersions and (b) coupling constants for interface phonon modes in three-interface heterostructure with layer dimensions a= 6 nm and b = 6 nm. The interface modes are grouped into the GaAs-like (dashed lines) and AlAs-like (solid lines) modes in the ascending order in frequencies. There are three phonon modes in each group labeled by: I(O) - inner (outer) interface modes; S(A) - symmetric (antisymmetric) modes in the limit $b>>a$.

Figure I.1.3.

Interface phonon potential distributions, $e\varphi_m(z)$, calculated for the three-interface heterostructures with different barrier widths: (a) $b = 12$ nm; (b) $b = 6$ nm; (c) $b = 3$ nm. Quantum well width is $a = 6$ nm; the value of phonon wave vector q is fixed at 0.4 nm^{-1}. Solid (dashed) lines refer to phonon modes in barrier (well) phonon energy range.

Figure I.1.4.

Scattering rates by the interface phonon modes as functions of the barrier width b at room temperature: (a) intrasubband 2-2 transitions; (b) intersubband 2-1 transitions. Initial electron kinetic energy in 2nd subband is $E_2 = 60$ meV. The combined scattering rates by both GaAs-like and AlAs-like modes are represented here.

Figure I.1.5.

Total scattering rates for intrasubband 1-1 transitions as function of electron kinetic energy in different phonon spectrum models. For the case when all the interface and confined modes of the heterostructure are taken into account, the curves are labeled by values of the barrier width $b = 3$, 6 and 12 nm.

Figure I.1.6.

Scattering matrix elements as functions of phonon wave vector q for intrasubband 1-1 transitions. The sum of all matrix elements (1) falls between the corresponding values for bulk well (2) and bulk barrier (3) phonons. All matrix elements are normalized to the value of bulk GaAs matrix element at small q. Initial electron kinetic energy in 1st subband is $E_1 = 60$ meV. Abbreviations: IS(A) - inner symmetric (antisymmetric) interface mode; O - outer interface mode; C - the total of barrier and well confined modes.

Figure I.2.1

Spectrum of electron excitation in a two-subband system with normal (a) and inverted (b) ordering of subband occupation. The continuum single-particle excitations of the initial state E_0 is represented by shaded regions and the dispersions of intrasubband (11,22) and intersubband (12,21) collective excitations are shown by heavy solid lines. Dashed lines illustrate the scattering of an external electron (e) by intersubband plasmon. In the insets we show electron-electron scattering events which are analogous to the electron-plasmon processes but are ineffective due to electron wave function orthogonality (a) or large momentum transfer (b).

Figure I.2.2

Approximate nonequilibrium distribution function for electrons in the first subband for subband depopulation time $\tau_{1out} = 1$ psec and two values of electron concentration n_2: a - $1 \times 10^{11} cm^{-2}$, b - $5 \times 10^{11} cm^{-2}$. The inset shows the occupation probability for electron states near the first subband bottom as a function of electron concentration n_2 for two different values of τ_{1out} (in psec).

Figure I.2.3

Down-shift and narrowing of the optical gain spectra due to the depolarization effect in a quantum well with inverted subband occupation. Dashed curves represent calculations neglecting the depolarization effect ($\alpha = 0$) for two values of electron concentration n_2: a - $5 \times 10^{10} cm^{-2}$; b - $4 \times 10^{11} cm^{-2}$. Solid curves labeled with the value of tunneling depopulation time τ_{1out} (in psec) illustrate the influence of the first subband bottom

filling on the gain spectrum at $n_2 \doteq 4 \times 10^{11} cm^{-2}$. The low-temperature value $\hbar\gamma = 1$ meV was taken for the polarization dephazing rate.

Figure II.1.1

Dependencies of threshold current density on temperature for three lasers with different doping profiles: undoped p-cladding/SCH interface (dotted curves, circles), moderately doped interface (dashed lines, triangles) and doped SCH region (solid lines, squares).

Figure II.1.2

Normalized slope efficiency as a function of temperature for lasers with three different doping profiles: undoped p-cladding/SCH interface (dotted curves, circles), moderately doped interface (dashed lines, triangles) and doped SCH region (solid lines, squares).

Figure II.1.3

Measured heterobarrier leakage current versus injection current for the lasers with undoped p-cladding/SCH interface (a) and doped SCH region (b) at 20^0C (circles), 50^0C (squares) and 80^0C (triangles).

Figure II.1.4

Dependencies of $1-J_L/J_I$ versus injection current for the lasers with undoped p-cladding/SCH interface (a) and doped SCH region (b).

Figure II.2.1

Schematic crossection of the fabricated structures before (a) and after (b) regrowth.

Figure II.2.2

Secondary Ion Mass Spectrometry (SIMS) concentration depth profiles of Zn and Si for structures before regrowth (a), 1 through 3, and for the same structures after regrowth (b), 4 through 6. The setback Δ is defined as the distance between the Zn-doping profile edge at a concentration of 5×10^{17} cm^{-3}, and the p-cladding/SCH interface at the concentration level of 5×10^{17} cm^{-3} (dashed line).

Figure II.2.3

Temperature dependence of the threshold current of the broad area laserts before regrowth (a) and after regrowth (b) . The insert of Fig. 3 shows the improvement of the characteristic temperature T_0 (temperature range of 10 to 80^0C) with doping at the heterointerface.

Figure II.2.4

The band diagram and quasi-Fermi levels for broad area lasers at high bias; p-doping profile corresponds to a setback $\Delta = 50$ nm. The free carrier density is shown in the lower panel.

Figure II.2.5

Ratio of the leakage current density to the injection current density at 25^0C as a function of setback. The experiment and theory are shown by solid and dashed lines, correspondingly.

Figure II.2.6

Optical loss measurements for CMBH structures with a cavity length of 300 μm. The values of Zn concentration in the middle of the active area are 3×10^{17} (open symbols) and 2.4×10^{18} cm^{-3} (closed symbols). The theory curves correspond to the $\Delta = -50$ nm.

Figure II.2.7

Simulated setback dependence of threshold current (a) and normalized efficiency (b) at 25^0C.

Figure II.2.8

The setback dependence of the threshold current (a) and normilized efficiency (b) at 25^0C for structures 1 through 6.

LIST OF PUBLICATIONS

1. M. Kisin, M. Stroscio, G. Belenky, S. Luryi. "Electron-plasmon resonance in quantum wells with inverted subband population". Physica E, in print (1999).

2. G.L.Belenky, C.L.Reynolds, Jr., D.V.Donetsky, G.E.Shtengel, M.Hybersen, M.A.Alam, G.A.Baraff, R.K.Smith, R.F.Kazarinov, J.D.Wynn, L.E.Smith, "Role of p-doping profile and regrowth on the static characteristics of 1.3 μm MQW InGaAsP/InP lasers. Experiment and modeling", IEEE J.of Quant.Electr., vol. 35, N10, p. 1515-1520 (1999).

3. M.S.Hybersen, M.A.Alam, G.E.Shtengel, G.L.Belenky, C.L.Reynolds, Jr., D.V.Donetsky, R.K.Smith, G.A.Baraff, R.F.Kazarinov, J.D.Wynn, and L.E.Smith, "Role of p-doping profile in InGaAsP multi-quantum well lasers: comparison of simulation and experiment", SPIE, vol.3625-60, p. 1-10 (1999).

4. G. Belenky, M. Dutta, V. Gorfinkel, G.I. Haddad, G.J. Iafrate, K.W. Kim, M. Kisin, S. Luryi, M.A. Stroscio, J.P. Sun, H.B. Teng, S.G. Yu. "Tailoring of optical phonon modes in nanoscale semiconductor structures: role of interface-optical phonons in quantum-well lasers", Physica B **263**, 462 (1999).

5. M. Kisin, M. Stroscio, G. Belenky, S. Luryi. "Electron-plasmon relaxation in quantum wells with inverted subband occupation". Appl. Phys. Lett., **73**, 2075 (1998).

6. M. Kisin, B. Gelmont, S. Luryi. "Boundary condition problem in the Kane model". Phys. Rev. B, **58**, 4605 (1998).

7. V. Gorfinkel, M. Kisin, S. Luryi. "Hot electrons and curves of constant gain in long wavelength quantum well lasers". Optics Express, **2**, 125 (1998).

8. M. Kisin, M. Stroscio, G. Belenky, V. Gorfinkel, S. Luryi. "Effects of interface phonon scattering in three-interface heterostructures". J. Appl. Phys., **83**, 4816 (1998).

9. D.V.Donetsky, G.L.Belenky, G.E.Shtengel, C.L.Reynolds, Jr., R.F.Kazarinov, and S.Luryi, "Temperature dependencies of output characteristics of 1.3 μm InGaAsP/InP lasers with different profile of p-doping", SPIE, vol.3283, p.423-431 (1998).

10. D.V.Donetsky, C.L.Reynolds, Jr., G.L.Belenky, G.E.Shtengel, R.F.Kazarinov, S.Luryi, "Optimization of p-doping profile of 1.3 μm InGaAsP/InP MQW lasers for high temperature operation", CLEO'98, San-Francisco, May 1998, OSA Technical Digest Series, vol.12, p.302 (1998).

11. G.L.Belenky, D.V.Donetsky, C.L.Reynolds, Jr., R.F.Kazarinov, G.E.Shtengel, S.Luryi, and J.Lopata, "Temperature performance of 1.3 μm InGaAsP-InP lasers with different profile of p-doping", IEEE Phot.Techn.Lett., vol.9, N12, p.1558-1560 (1997).

12. D.V.Donetsky, G.L.Belenky, C.L.Reynolds, Jr., R.F.Kazarinov, S.Luryi, "Effect of p-doping on carrier leakage and characteristic temperature To of 1.3 μm strained InGaAsP/InP multiple quantum well lasers", CLEO'97, Baltimore, May 1997, OSA Technical Digest Series, vol.11, p.157 (1997).

38

LIST OF PARTICIPATING SCIENTIFIC PERSONNEL

Dr. Gregory Belenky, Associate Professor

Dr. Mikhail Kisin, Senior Research Scientist

D. Donetsky, Graduate Student

L. Shterengas, Graduate Student

Dr. Serge Luryi, Leading Profesor

BIBLIOGRAPHY

Agrawal G.P. and N.K. Dutta "Long-Wavelength Semiconductor Lasers", Van Nostrand Reinhold, New-York, 1986.

Alam M.A., M.S. Hybertsen, R.K. Smith, G.A. Baraff, M.R. Pinto, *SPIE,* **2994**, 709 (1997)

Allen S.J., D.C. Tsui, and B. Vinter, *Solid State Comm.* **20**, 425 (1976).

Ando T., *J. Phys. Soc. Jpn.* **44**, 475 (1978).

Anthony P.J., N.E.Schumaker, *IEEE Electron Device Lett.* **EDL-1**, 58, (1980).

Belenky G.L., R.F.Kazarinov, J.Lopata, S.Luryi, T. Tanbun-Ek, and P.Garbinski, *IEEE Trans. Electron Dev.*, **42**, 215 (1995).

Belenky G.L., L. Reynolds, R.F.Kazarinov, S.Swamatanian, S.Luryi, J.Lopata, *IEEE J. of Quant. Electron.*, **32**, 1450 (1996).

Belenky G.L., D.V. Donetsky, C.L.Reynolds Jr., R.F.Kazarinov, G.E.Shtengel, S.Luryi and J. Lopata, *IEEE Phot.Techn.Lett.,* **9**, 1558 (1997).

Bemussi A.A., H.Temkin, R.A.Logan, D.C.Coblentz, *Appl.Phys.Lett.*, **66** (1), 67 (1995).

Bhatt A.R., K.W. Kim, M.A. Stroscio, and J.M. Higman, *Phys. Rev. B*, **48**, 14671 (1993).

Capasso F., C. Gmachl, A. Tredicucci, A.L. Hutchinson, D.L. Sivco, A.Y. Cho. *Optics & Photonics News*, **10**, 32 (1999).

Capasso F., J.Faist, C.Sirtori, D.L.Sivco, A.L.Hutchinson, A.Y.Cho, *Nature* **387**, 777 (1997).

Capasso F., J. Faist, C. Sirtori, *J. Math. Phys.* **37**, 4775 (1996).

Chen T.R, S.Margalit, U.Koren, K. L.Yu, L.Chiu, A.Hasson,and A..Yariv, *Appl.Phys.Lett.*, **42**, 1000 (1983).

Constantinou N.C., *J. Phys.: Condens. Matter*, **3**, 6859 (1991).

Das Sarma S., In *Hot Carriers in Semiconductor Nanostructures*, ed. by J. Shah (Academic, NY), p.53 (1996).

Donetsky D.V., C.L.Reynolds Jr, G.L.Belenky, G.E.Shtengel, R.F.Kazarinov, S.Luryi, *CLEO-98 Technical Digest*, San-Francisco, 302 (1998).

Educato J.L., J.-P. Leburton, P. Boucand, P. Vagos, and F.H. Julien, *Phys. Rev. B*, **47**, 12949 (1993).

Elesin V.F., Yu. V. Kopaev, *JETP*, **81**, 1192 (1995).

Faist J., F. Capasso, D.L. Sivco, C. Sirtori, A.L. Hutchinson, A.Y. Cho, *Science* **264**, 553 (1994).

Faist J., F. Capasso, C. Sirtori, D.L. Sivco, A.L. Hutchinson, M.S. Hybertsen and A.Y. Cho, *Phys. Rev. Lett.*, **76**, 411 (1996).

Garbuzov D., G.-J.Shian, V.Bulovic, M.Boroditsky, C.-P.Chao and S.R.Forrest, *Appl.Phys.Lett.*, **66** (11), 1307 (1995).

Gauthier-Lafaye O., P. Boucaud, F.H. Julien, S. Sauvage, S. cabaret, J.-M. Lourtioz, V. Thierry-Mieg, R. Planel, *Appl. Phys. Lett.* **71**, 3619 (1997).

Gmachl C., A. Tredicucci, F. Capasso, A.L. Hutchinson, D.L. Sivco, J.N. Baillargeon, and A.Y. Cho, *Appl. Phys. Lett.* **72**, 3130 (1998).

Gorfinkel V., S. Luryi and B. Gelmont, *IEEE J. Quant. Electron*, **32**, 1995 (1996).

Henry C.H., R.A. Logan, F.R. Merritt and J.P. Luongo, *IEEE J. Quant. Electron*, **19**, 947 (1983).

Huang K., and B. Zhu, *Phys. Rev. B*, **38**, 13377 (1988).

Hybertsen M.S., M.A. Alam, G.A.Baraff, A.A. Grinberg, and R.K. Smith, *SPIE*, **3283**, 375 (1998)

Hybertsen M.S., M.A. Alam, R.K. Smith, G.A. Baraff, and M.R. Pinto, in *Proc. of the IEEE Twenty-Fourth Internantional Symposium on Compound Semiconductors*, M. Melloch and M.A. Reed eds, Institute of Physics Publishing, Philidelphia, 625 (1998).

Jain J.K., and S.Das Sarma, *Phys. Rev. Lett.* **62**, 2305 (1989).

Kazarinov R.F. and M.R. Pinto, *IEEE J. Quant. Electron.*, **30** (1), 49, (1994).

Kim K.W., A.R. Bhat, M.A. Stroscio, P.J. Turley, and S.W. Teitsworth, *J. Appl. Phys.* **72**, 2282 (1992).

Kisin M., V.B. Gorfinkel, M. A. Stroscio, G. Belenky, S. Luryi, *J. Appl. Phys.* **82**, 2031 (1997).

Kisin M., M. Stroscio, G. Belenky, V. Gorfinkel and S. Luryi, *J. Appl. Phys.* **83**, 4816 (1998).

Mori N., T. Ando, *Phys. Rev. B,* **40**, 6175 (1989).

Morton P.A., D.A.Ackerman, G.E.Shtengel, R.F.Kazarinov, M.S.Hybertsen, T.Tanbun-Ek, R.A.Logan, A.M.Sergent, *IEEE Phot.Techn.Lett.,***7** (8), 833 (1995).

Nakahara K., K.Uomi, T.Tsuchiya, A.Niwa, T.Haga, and T.Taniwatari, *IEEE J. Selected Topics in Quant.Electron.,* **3** (2), 166 (1997).

Niwa A., T.Ohtoshi, K.Uomi, K.Nakahara, *IEEE Phot.Techn.Lett.,***8** (3), 328 (1996).

Register L.F., Phys. Rev. B, **45**, 8756 (1992).

Rücker H., E. Molinari and P. Lugli, *Phys. Rev. B,* **45**, 6747 (1992).

Seki S., K.Yokoyama, *Appl.Phys.Lett.,***77** (10), 5180 (1995a)

Seki S., H.Oohasi, H.Sugiura, T.Hirono and K.Yokogama, *Appl.Phys.Lett.,* **67** (8), 1054 (1995b).

Schubert E.F., S.W.Downey, C.Pinzane, and A.B.Emerson, *Appl.Phys.A.,* **60**, 525 (1995).

Shtengel G.E., D.A.Ackerman, *Electron Lett.*, **31**, 1157 (1995)

Sirtori C., J. Faist, F. Capasso, D.L. Sivco, A.L. Hutchinson, S.N. George Chu and A.Y. Cho, *Appl. Phys. Lett.* **68**, 1745 (1996).

Stroscio M.A., *J. Appl. Phys.* **80**, 6864 (1996).

Su C.B., V.Lanzisera, *Appl.Phys.Lett.,* **45**, 1302 (1984).

Sun G., J.B. Khurgin, *IEEE J. Quantum Electron.* **29**, 1104 (1993).

Swamatanian V, C.L.Reynolds, Jr., and M.Geva, *Appl. Phys. Lett.* **66**, 2685 (1995).

Swamatanian V., C.L.Reynolds,Jr., and M.Geva, *Electron Lett.* **32**, 661 (1996).

Turley P.J., and S.W. Teitsworth, *Phys. Rev. B*, **50**, 8423 (1994).

Vinter B., *Phys. Rev. B*, **15**, 3947 (1977).

Warburton R.J., C. Gauer, A. Wixforth, J.P. Kotthaus, B. Brar and H. Kroemer, *Superlattices and Microstructures*, **19**, 365 (1996).

Yamanaka T., Y.Yoshikuni, K.Yokoyama, W.Lui, S.Seki, *IEEE J. Quant. Electron.*, **29** (6), 1609 (1993).

Yu SeGi, K.W. Kim, M.A. Stroscio, G.J. Iafrate, J.P. Sun, and G.I. Haddad, *J. Appl. Phys.* **82**, 3363 (1997).

Zaluzny M., *Phys. Rev. B* **43**, 4511 (1991).

Zhang L. and D.A.Ackerman, *IEEE J. Quant. Electron.*, **31**(11), 1974 (1995).

Zilko J.L., L.J.P. Ketelsen, Y.Twu, D.P.Wilt, S.G. Napholtz, J.P.Blaha, K.E.Strege, V.G. Riggs, D.L. Van Haren, S.Y.Leung, P.M.Nitzsche, J. Long, C.B.Roxlo, G.Przyblek, J.Lopata, M.W.Focht and L.A.Koszi, Heterostructure Distributed Feedback (CMBH-DFB) Lasers *IEEE J. Quantum Electron.* **25**(10), 2091 (1989).
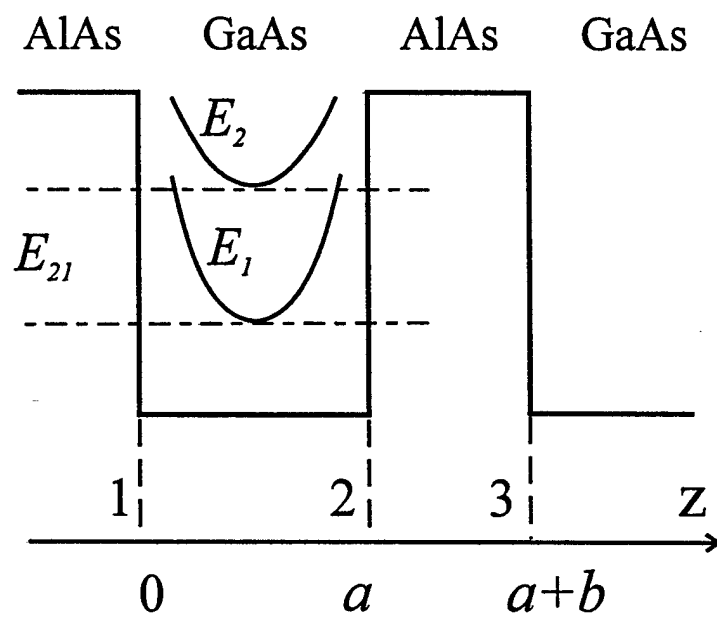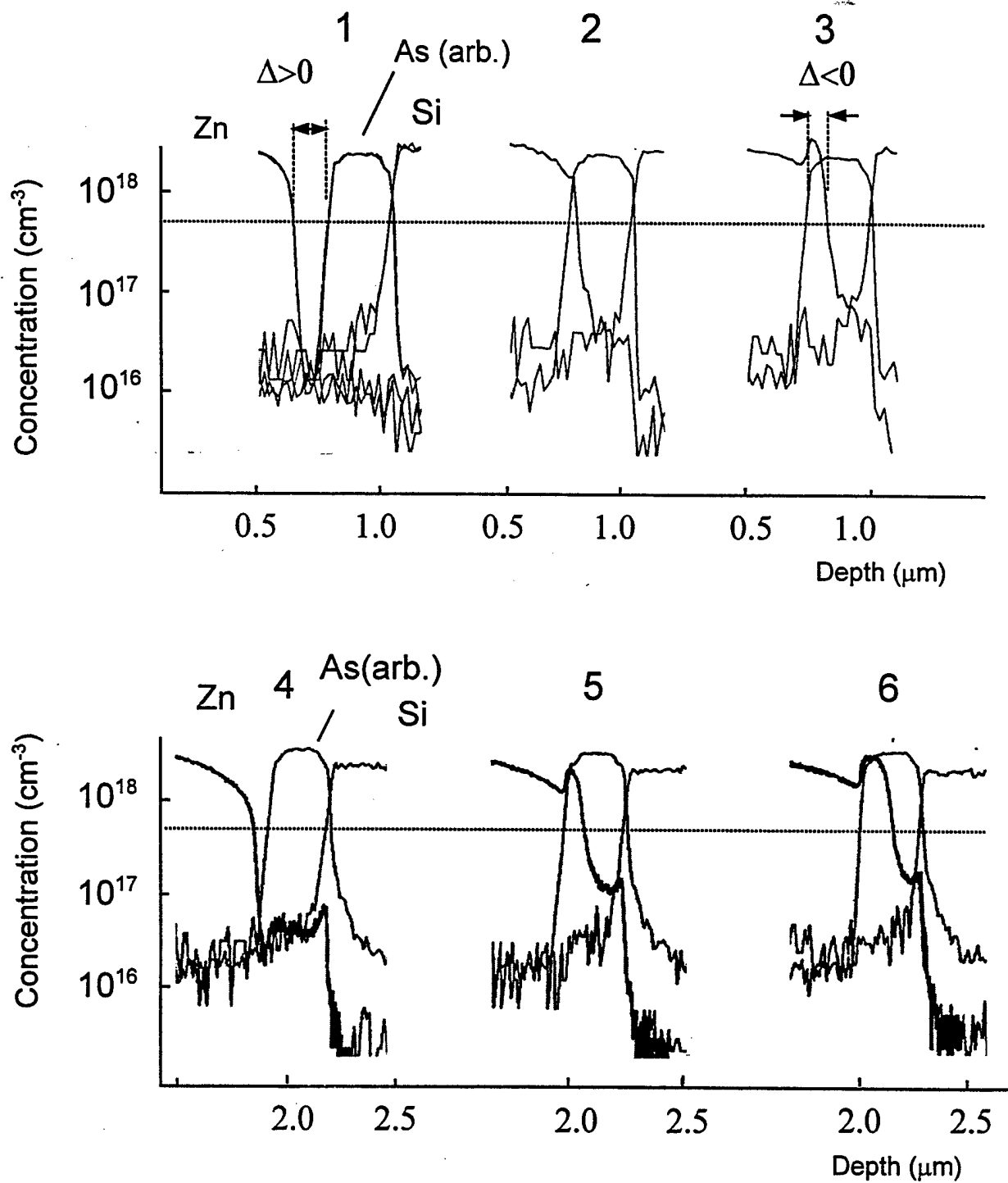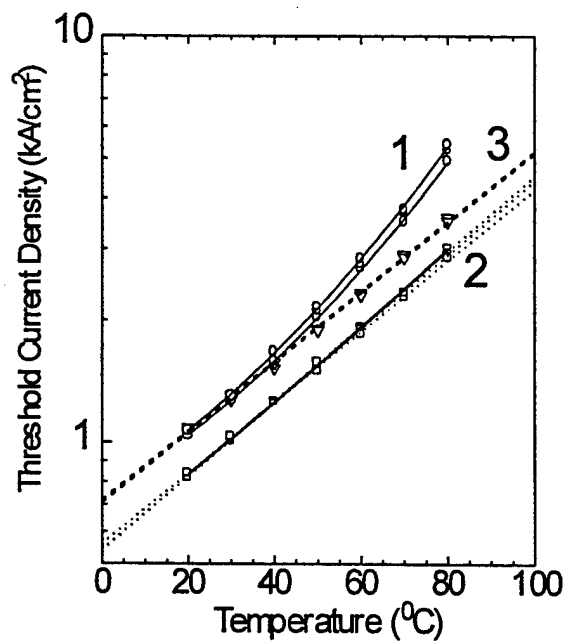
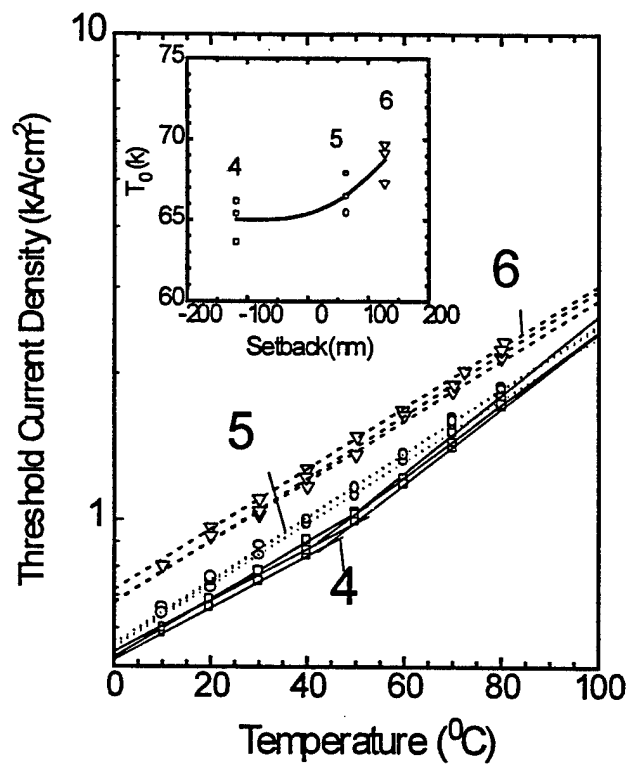Fig. I.1.1
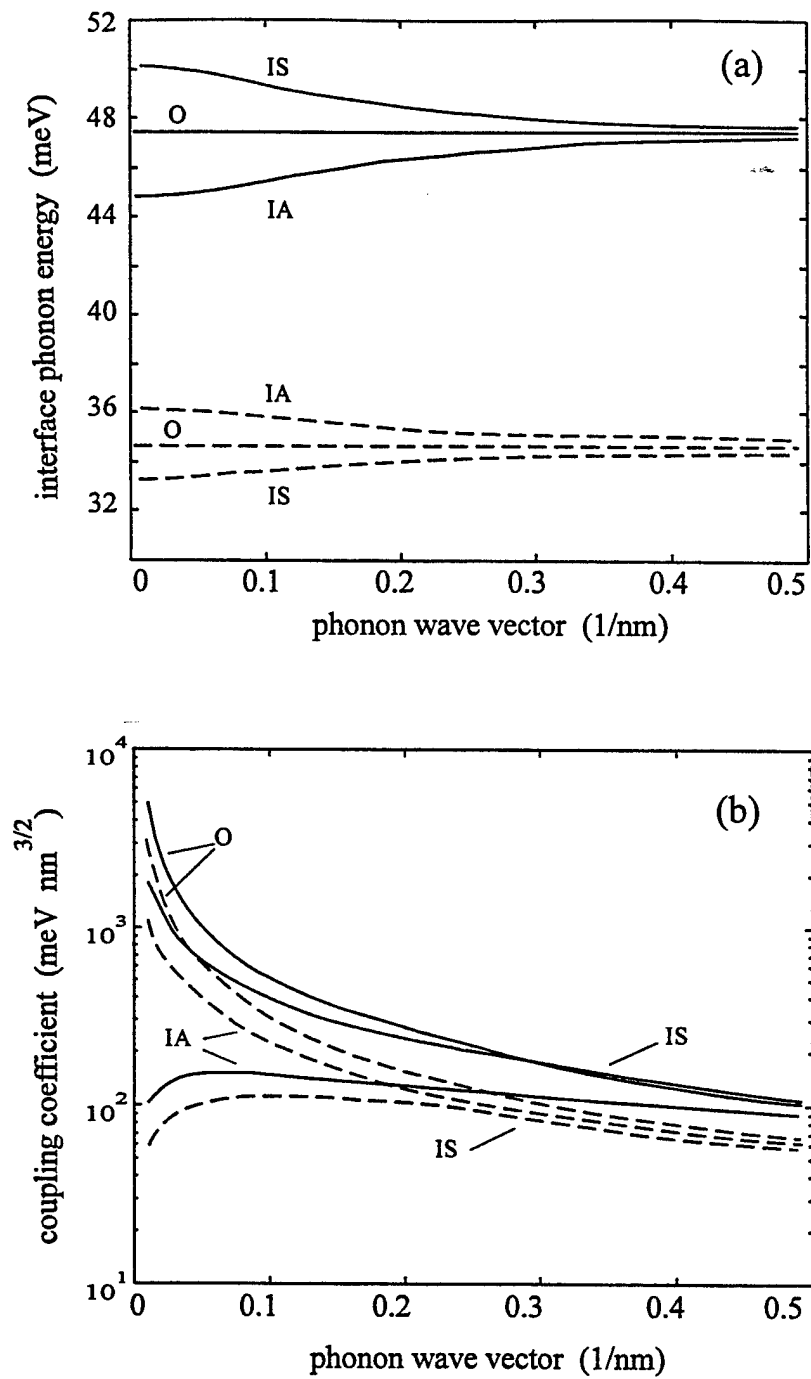
Fig. I.1.2
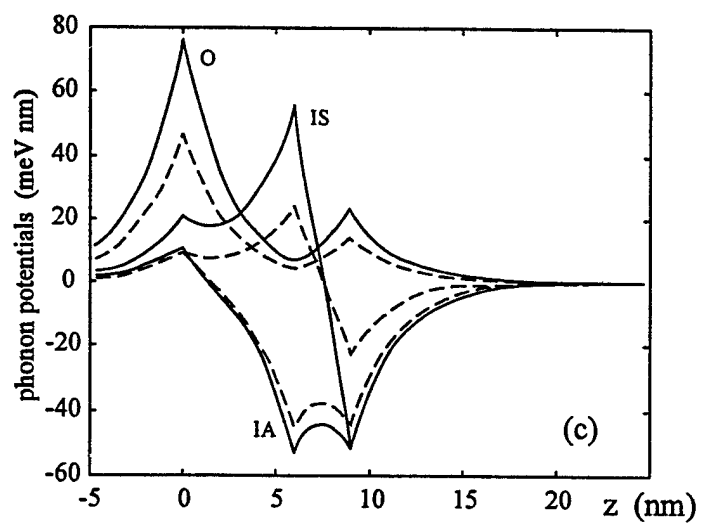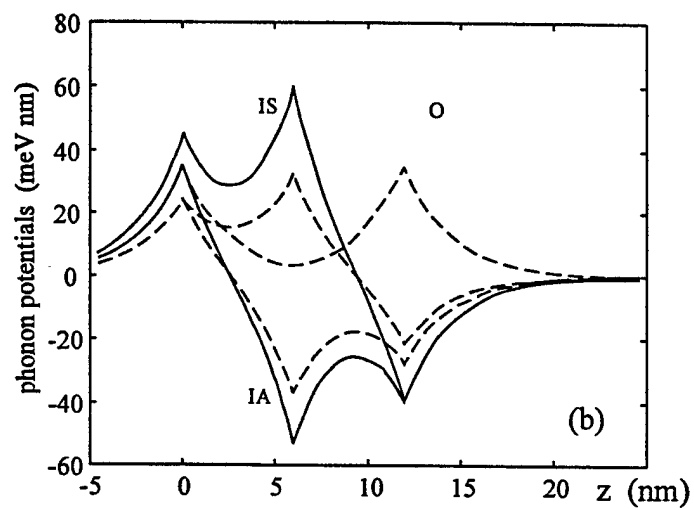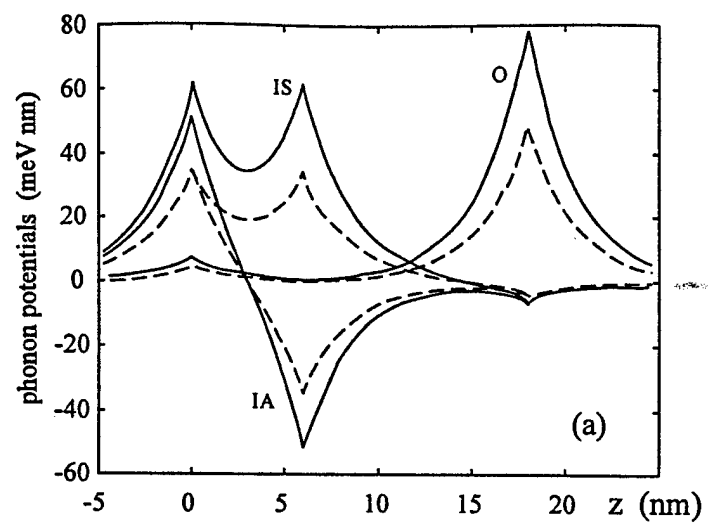
Fig. I.1.3
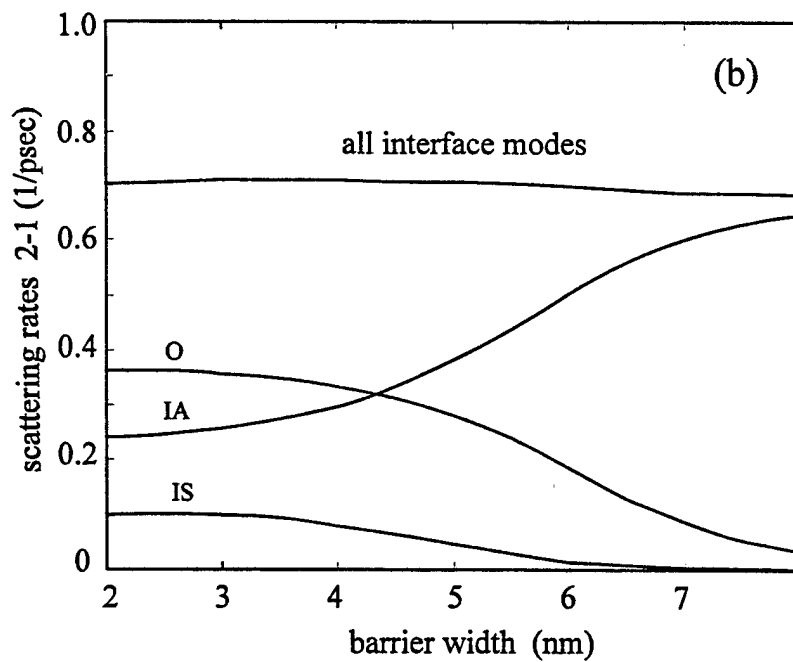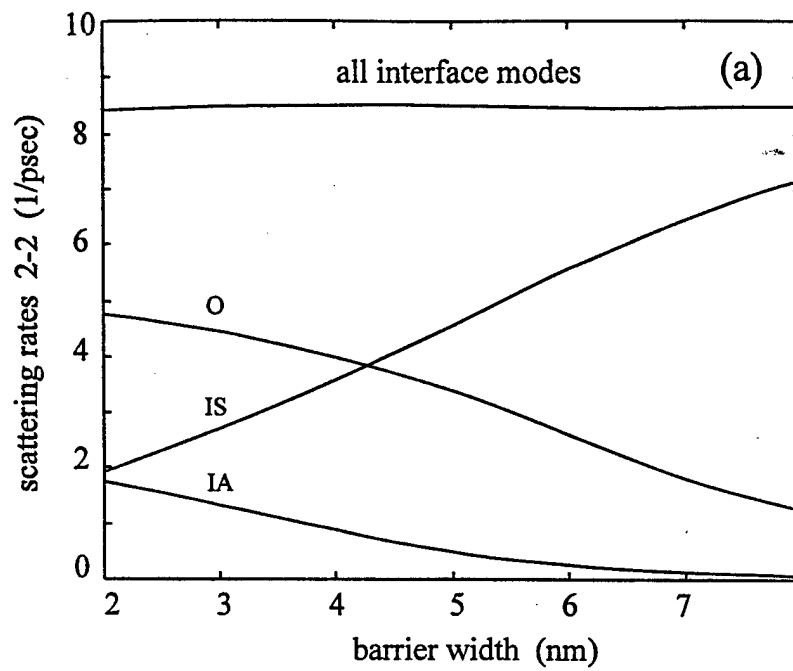
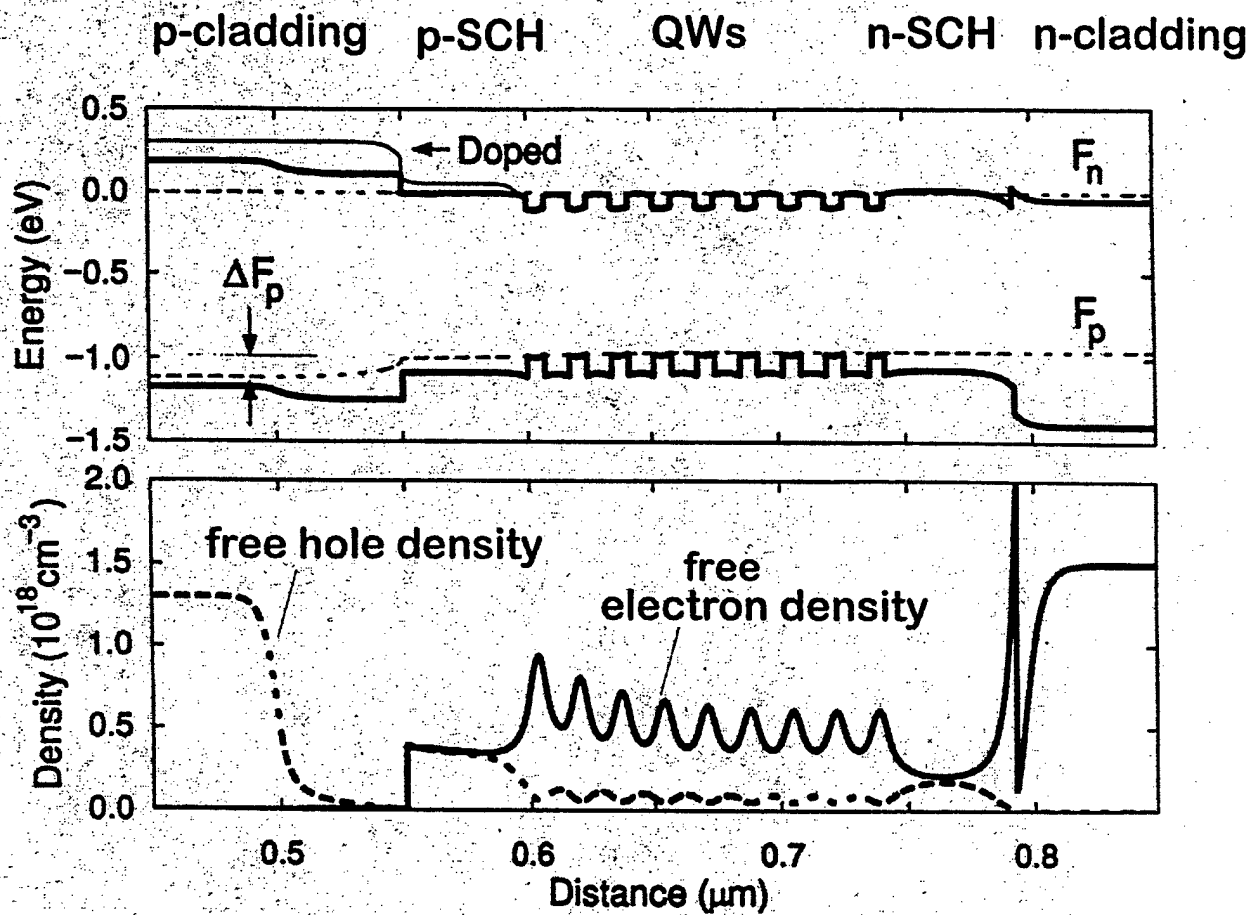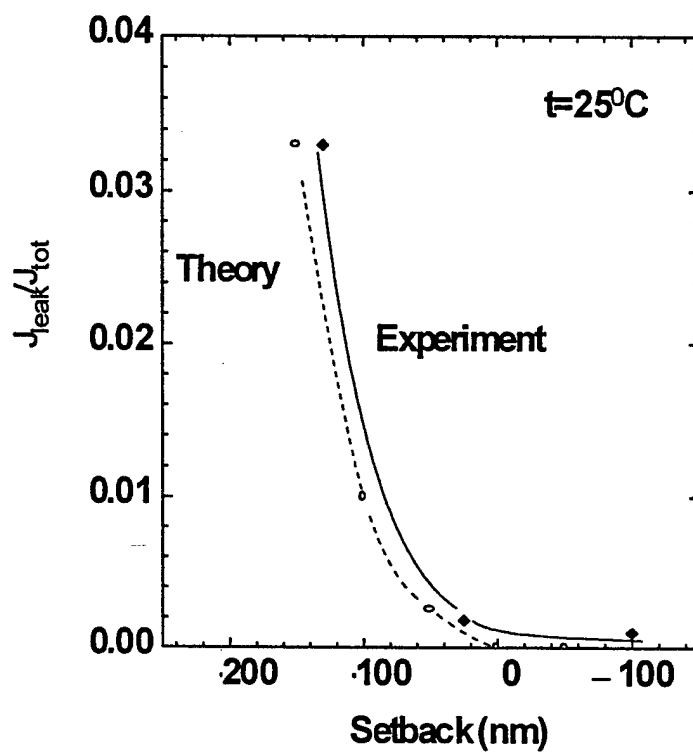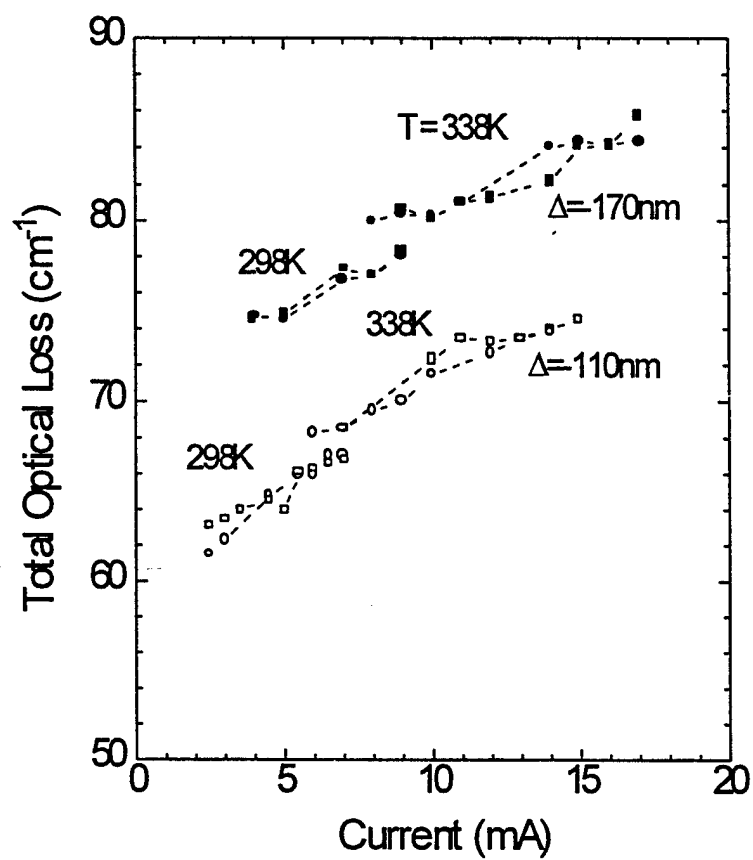Fig. I.1.4
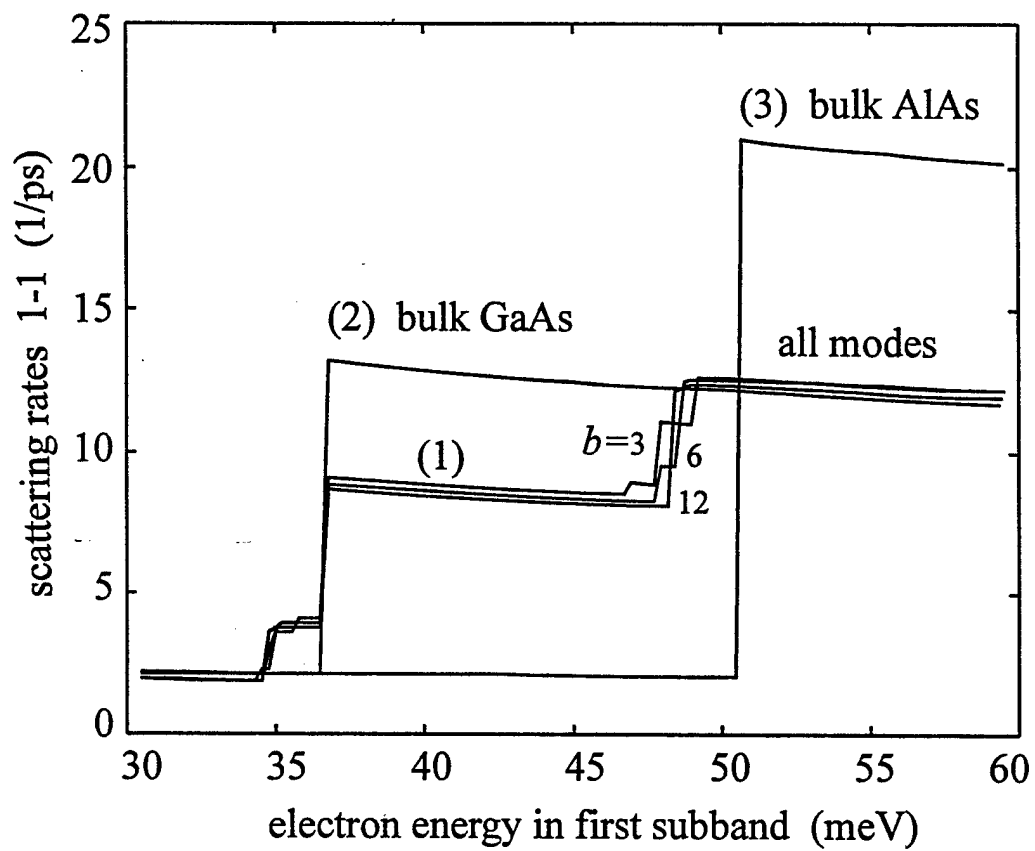
Fig. I.1.5
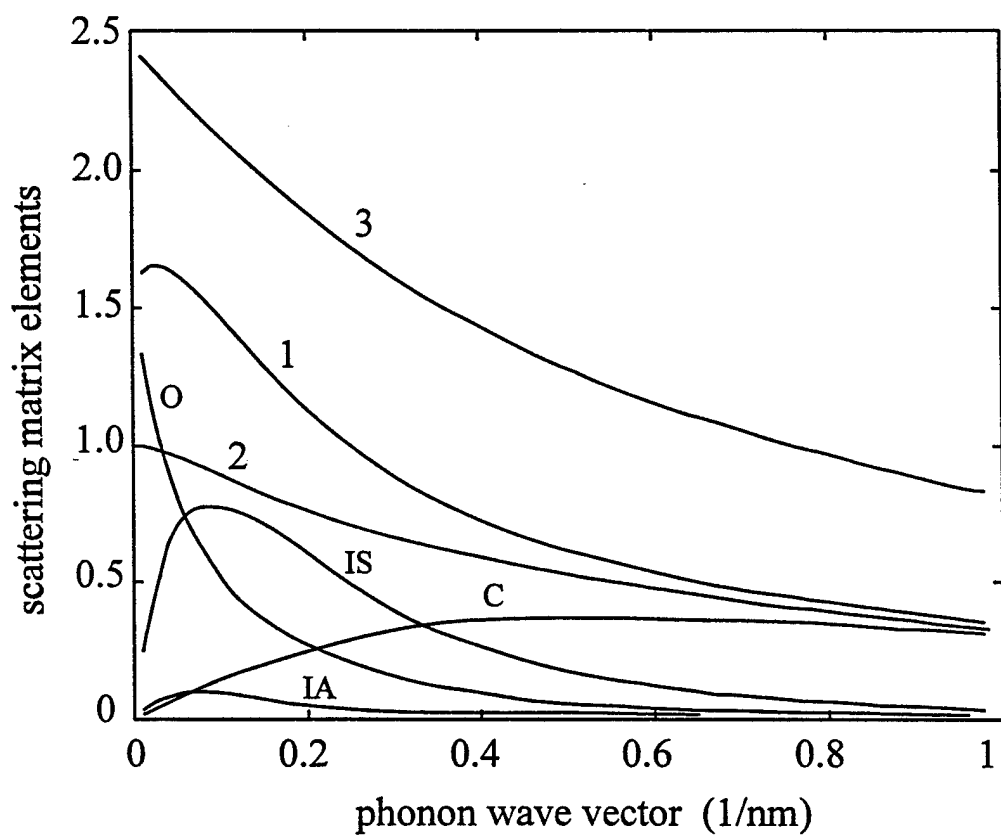
Fig. I.1.6
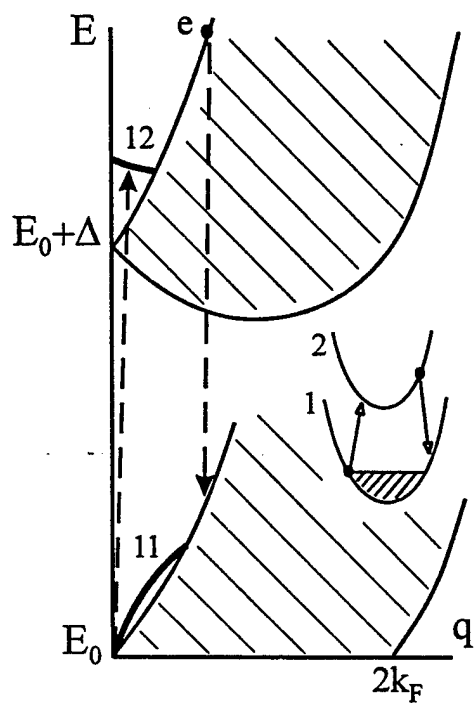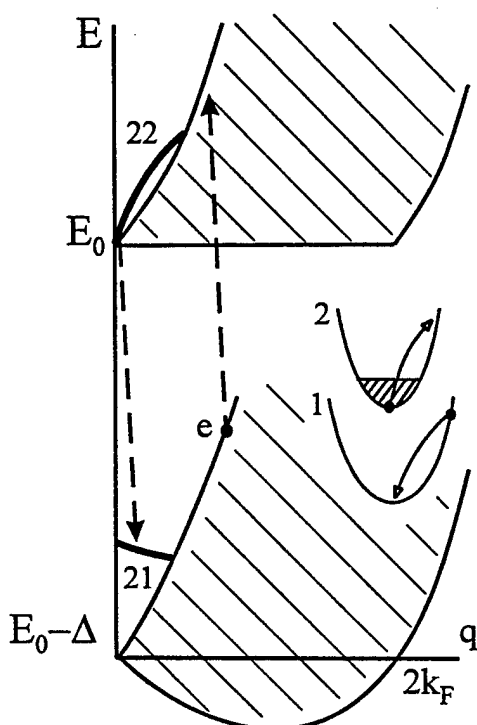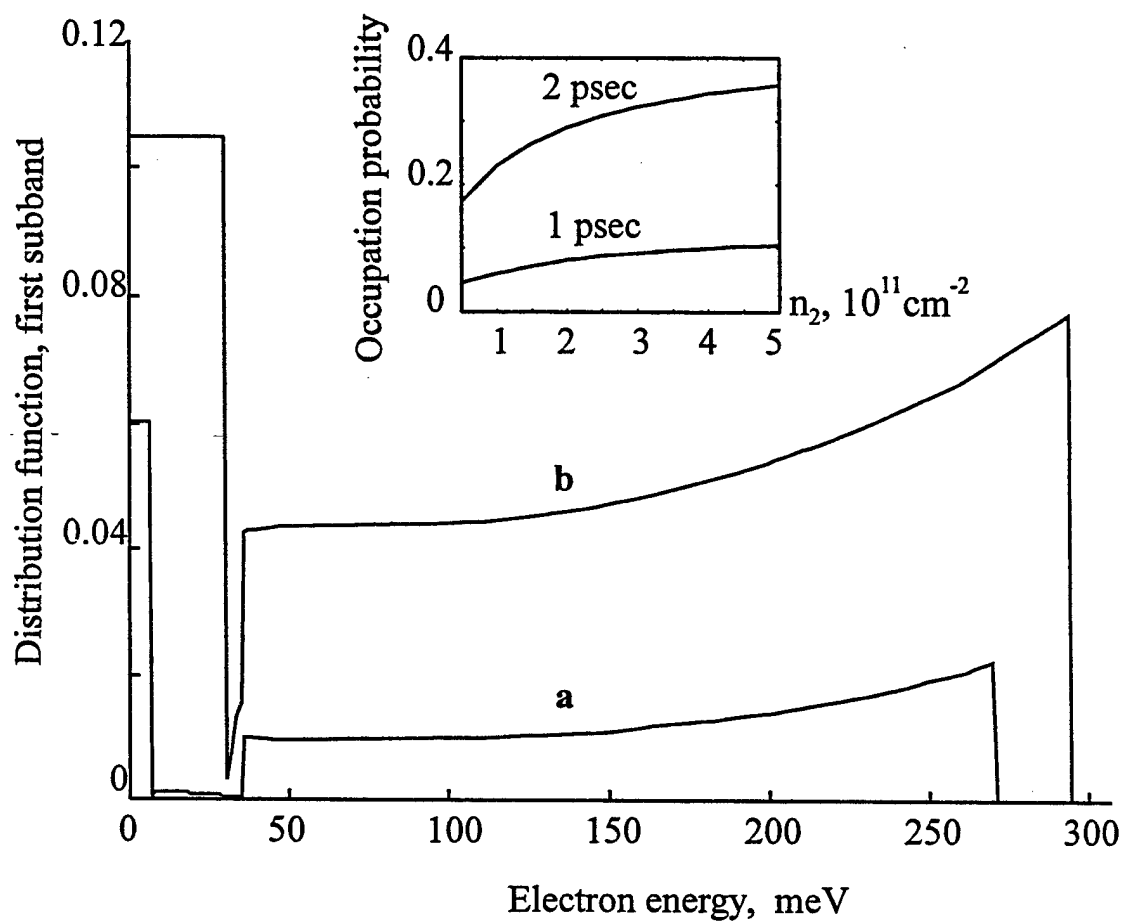
Fig. I.2.1

Fig. I.2.2

Fig. I.2.3

Fig. II.1.1

Fig. II.1.2

Fig. II.1.3

(a)

Injection Current Density J_i (kA/cm^2)

(b)

Injection Current Density J_i (kA/cm^2)

Fig. II.1.4

Left structure:

p-contact

InP p-cladding
0.6 μm

SCH 50 nm

9 QWs 70 A,
barriers 100 A

SCH 50 nm

InP n-cladding 0.75 μm

InP substrate

InP n-contact

Right structure:

p-contact

InP p-cladding
1.8 μm

SCH 50 nm

9 QWs 70 A,
barriers 100 A

SCH 50 nm

InP n-cladding 0.75 μm

InP substrate

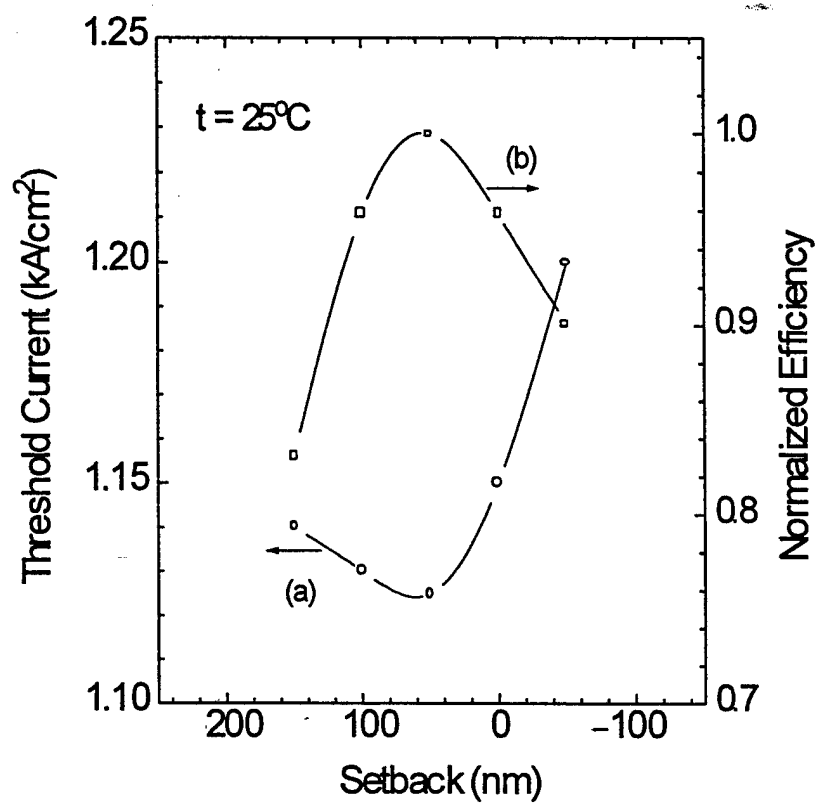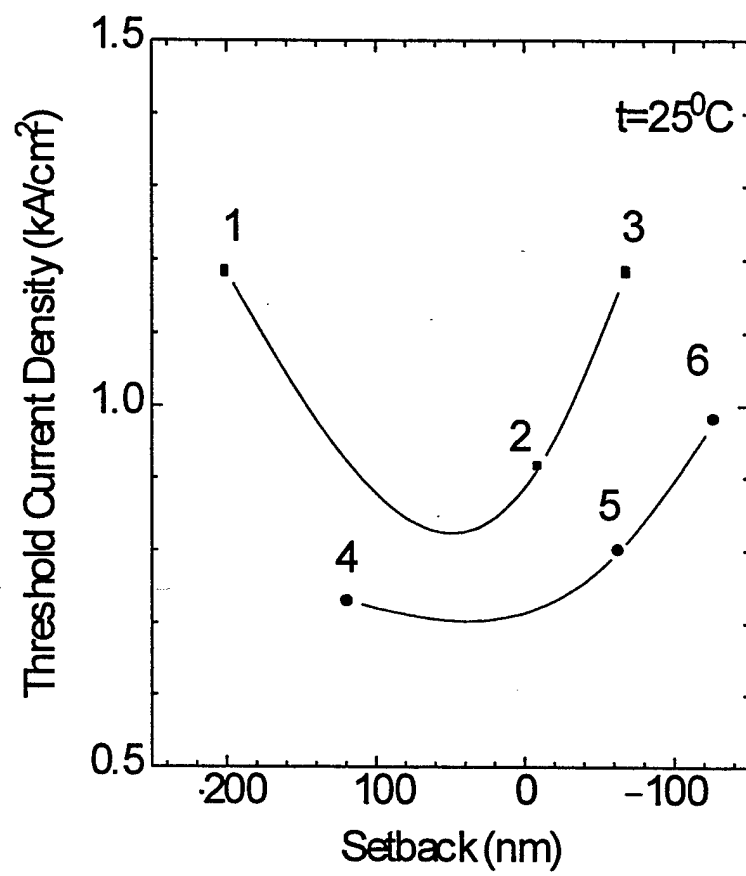InP n-contact
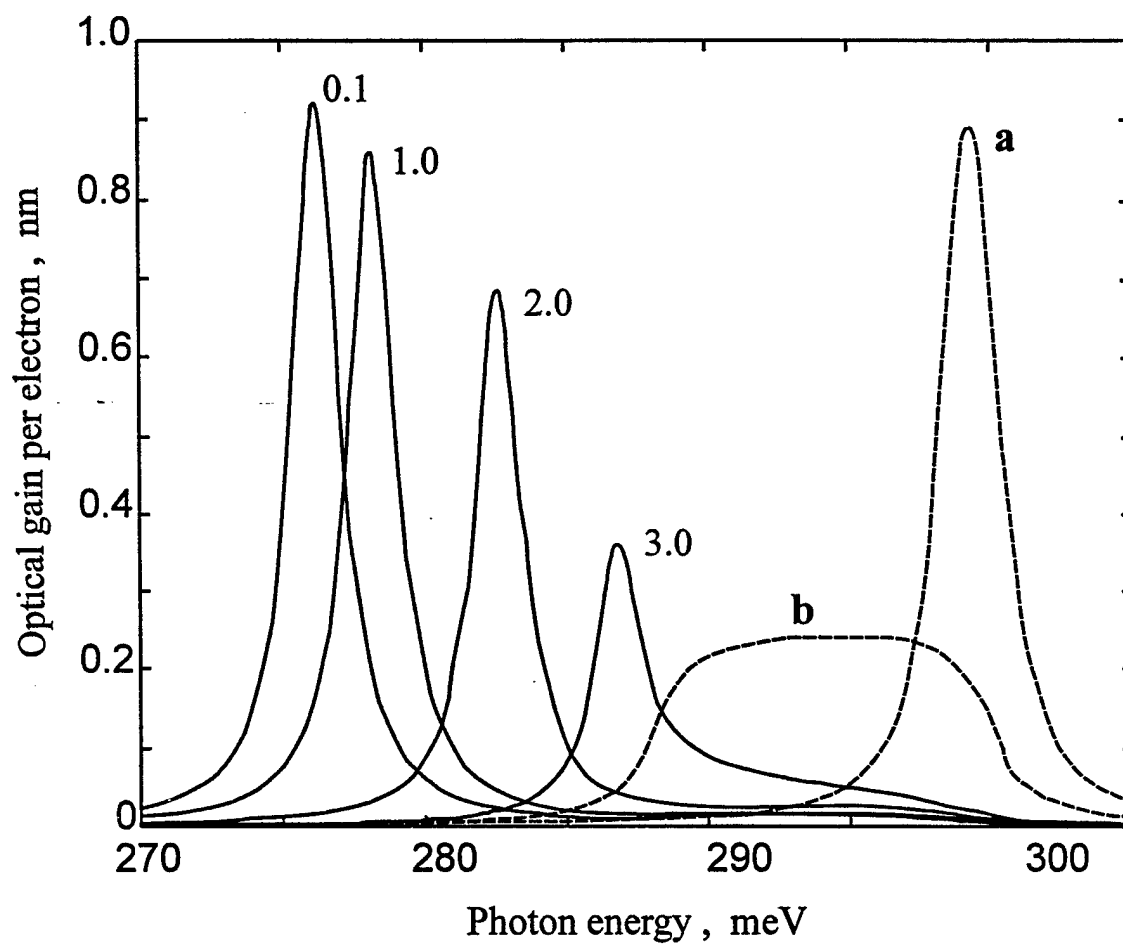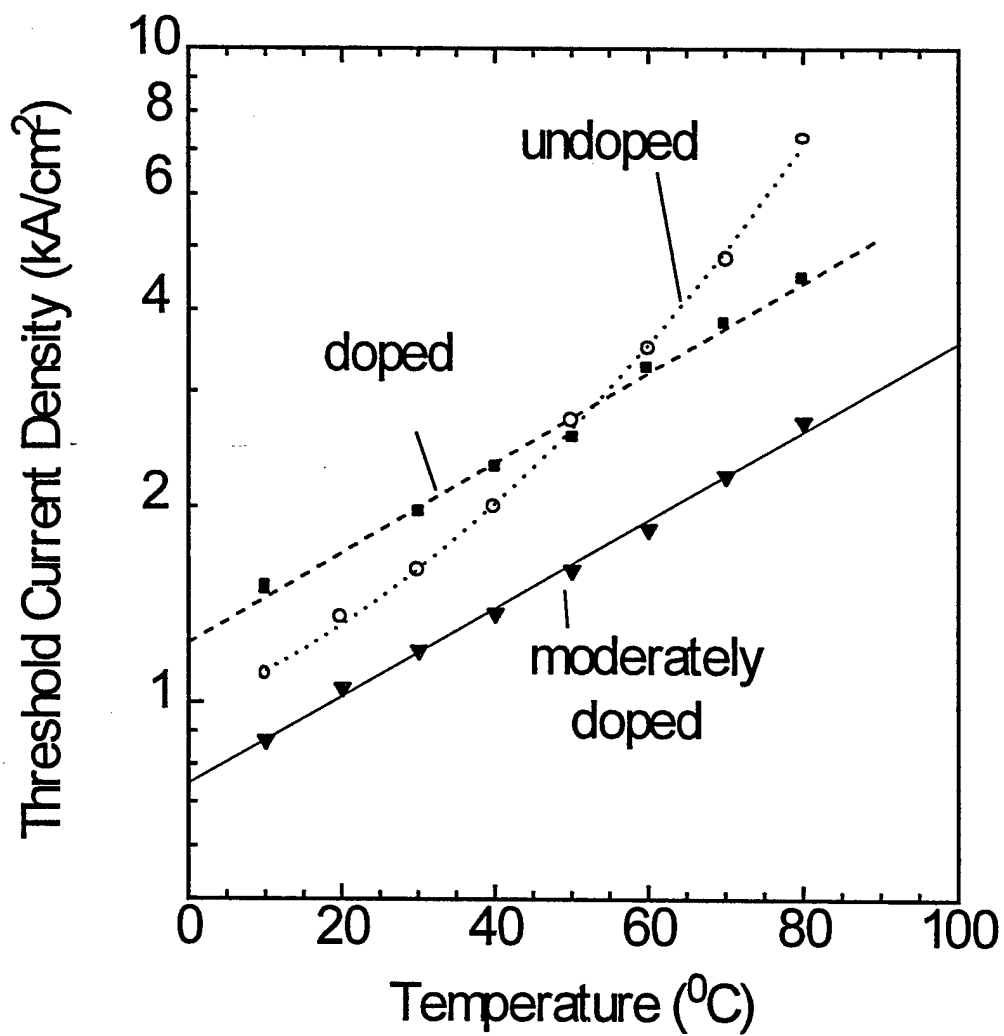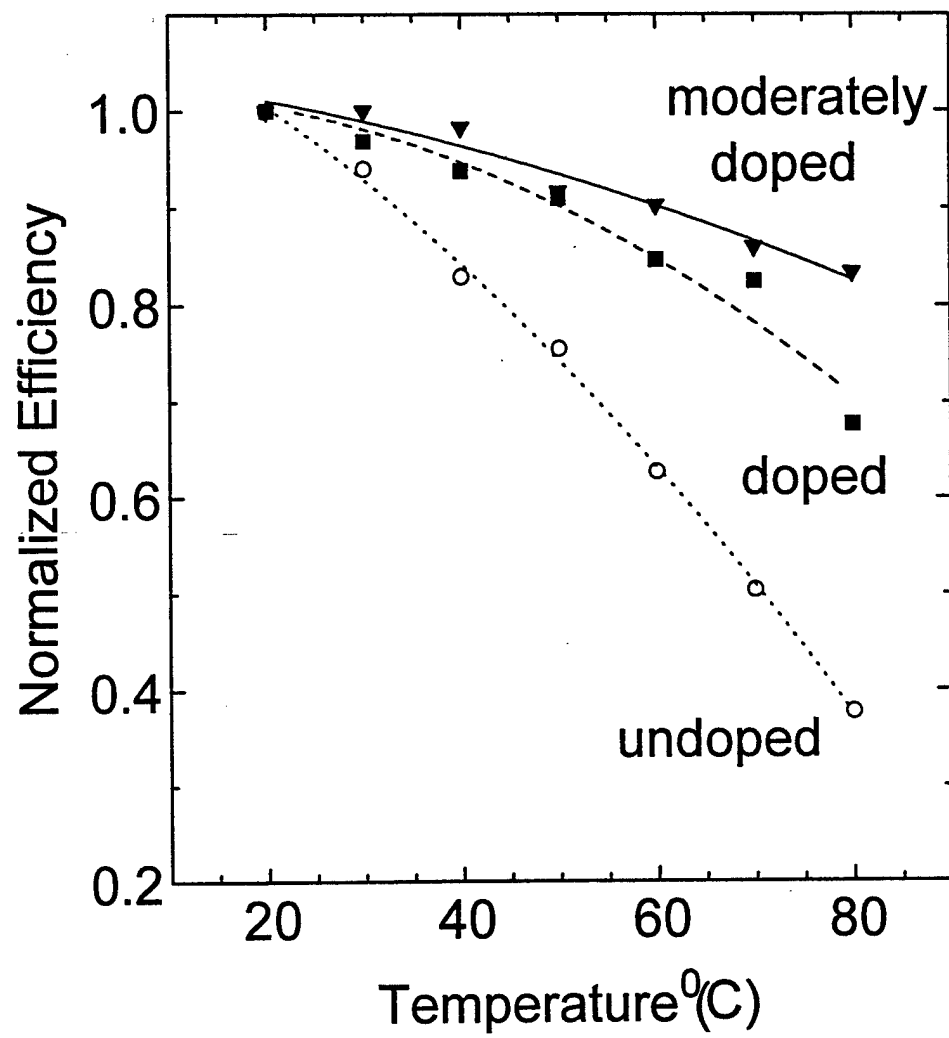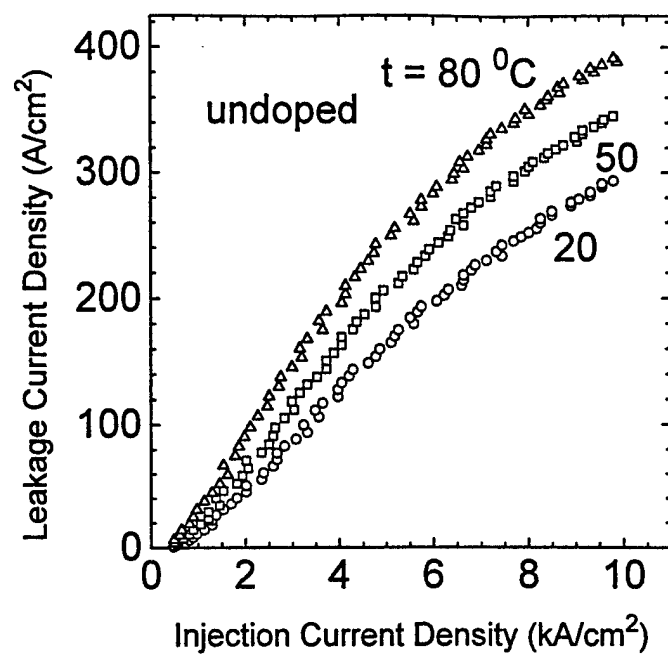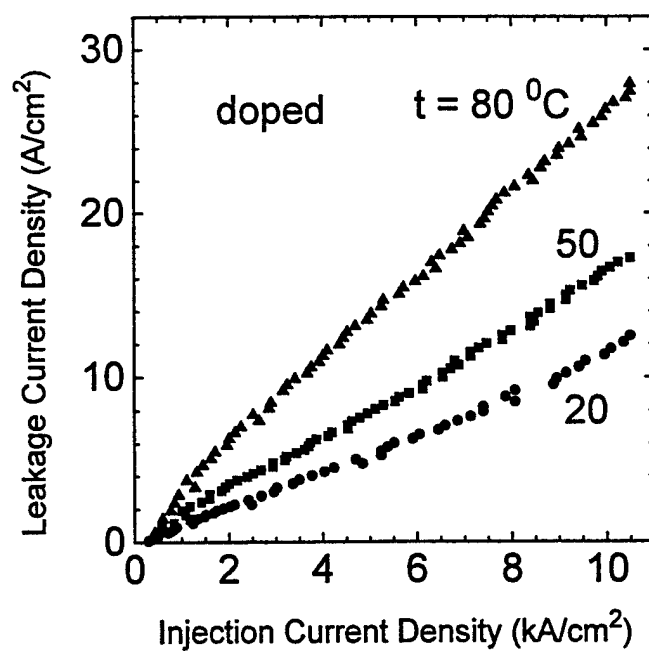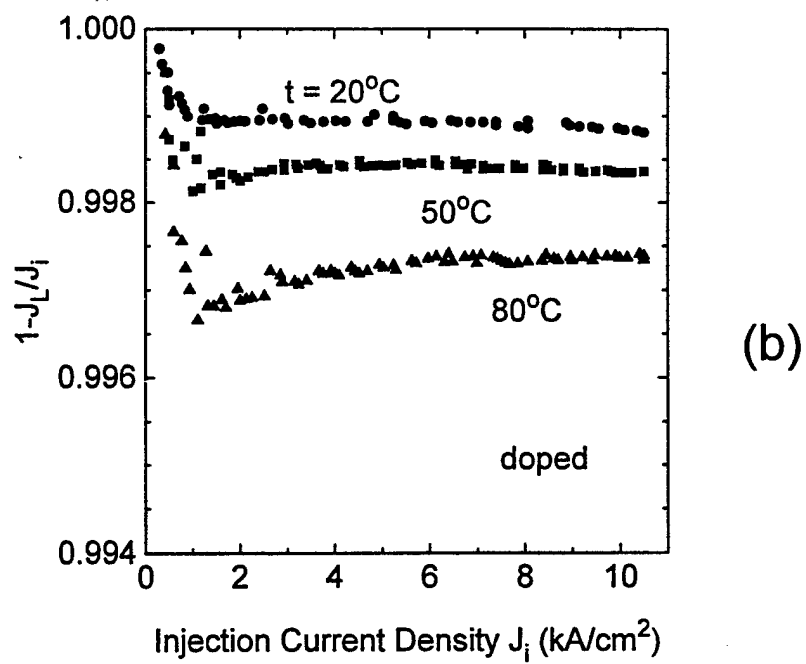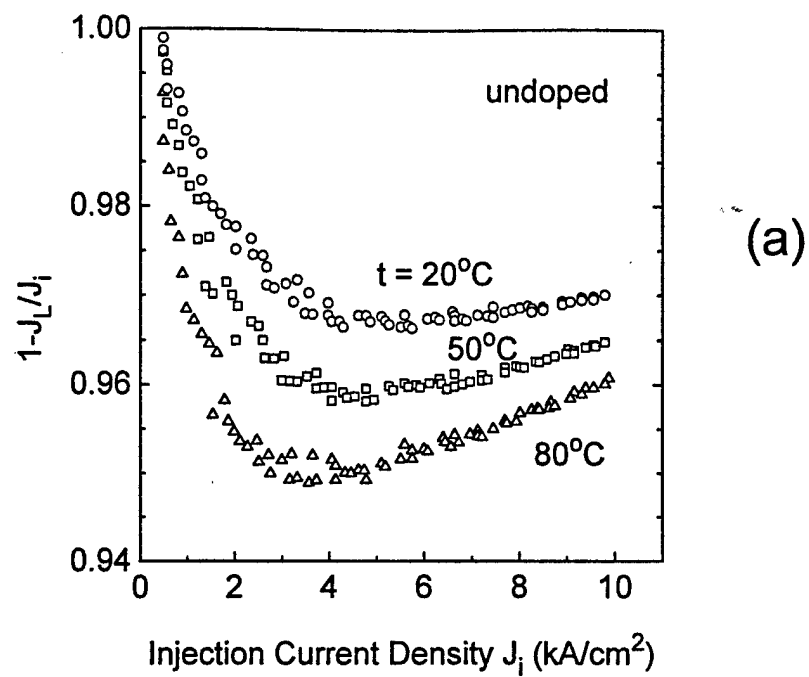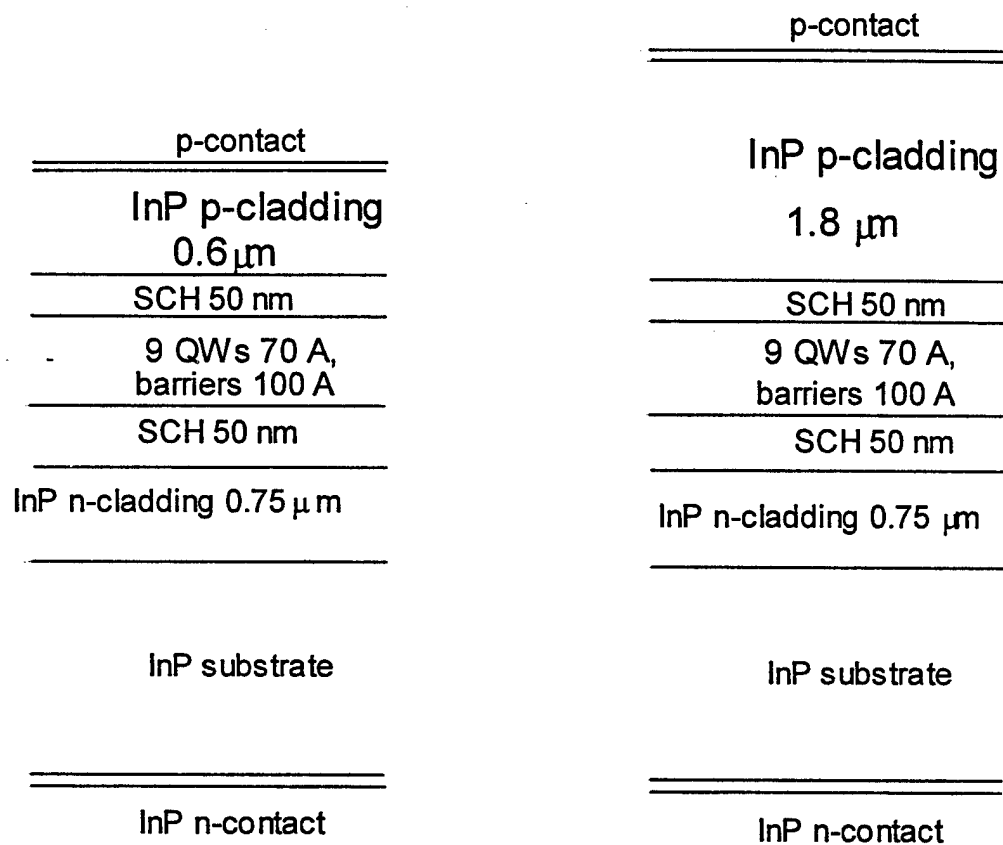
Fig. II.2.1

Fig. II.2.2

Fig. II.2.3

Fig. II.2.4

Fig. II.2.5

Fig. II.2.6

Fig. II.2.7

Fig. II.2.8a

Fig. II.2.8b